CFD Investigation into the Relationship Between Aerodynamic Drag and the Addition of Flow-Modifying Pods Appended to a Simplified Generic Tractor-Trailer

Marcus Boyd
School of Engineering
University of the West of England (UWE)
Bristol, UK
marcus2.boyd@live.uwe.ac.uk

Abstract

In the following research, an aerodynamic analysis of a simplified Class 8 tractor-trailer geometry was conducted using Computational Fluid Dynamics (CFD), including an investigation into the relationship between drag and the addition of AeroHance pods appended to the model, with various pod configurations considered. The AeroHance pod shape is inspired by whale tubercles, which are present on the flippers of the Humpback whale, with the purpose of the pods being the reduction in aerodynamic drag of automotive vehicles.

The methodology comprised of three main objectives: a) CFD setup validation with the use of experimental data obtained by [1], b) Full-scale tractor-trailer analysis without AeroHance pods appended to gather baseline data in open-road conditions, and c) The analysis of various pod configurations to find the optimum arrangement in terms of drag reduction.

The findings of this report display that AeroHance pods can offer an effective solution to the reduction of aerodynamic drag on Class 8 tractor-trailers, reducing the total drag force by up to 2.12% via the reduction in strength of vortices in the wake, thus leading to an increase in base pressure. At typical highway speeds, this corresponds to a fuel saving of approximately 1.38%. A case study conducted as part of this research found that under realistic operating conditions at an average driving speed of 50 mph, an increase in fuel economy of approximately 1.04% could be expected. For a 10-vehicle fleet of Class 8 tractor-trailers, this results in an annual saving of around \$4136.49 for operations within the United States, or £7235.56 in the United Kingdom, with a reduction in CO_2 emissions of roughly 11,005 kg.

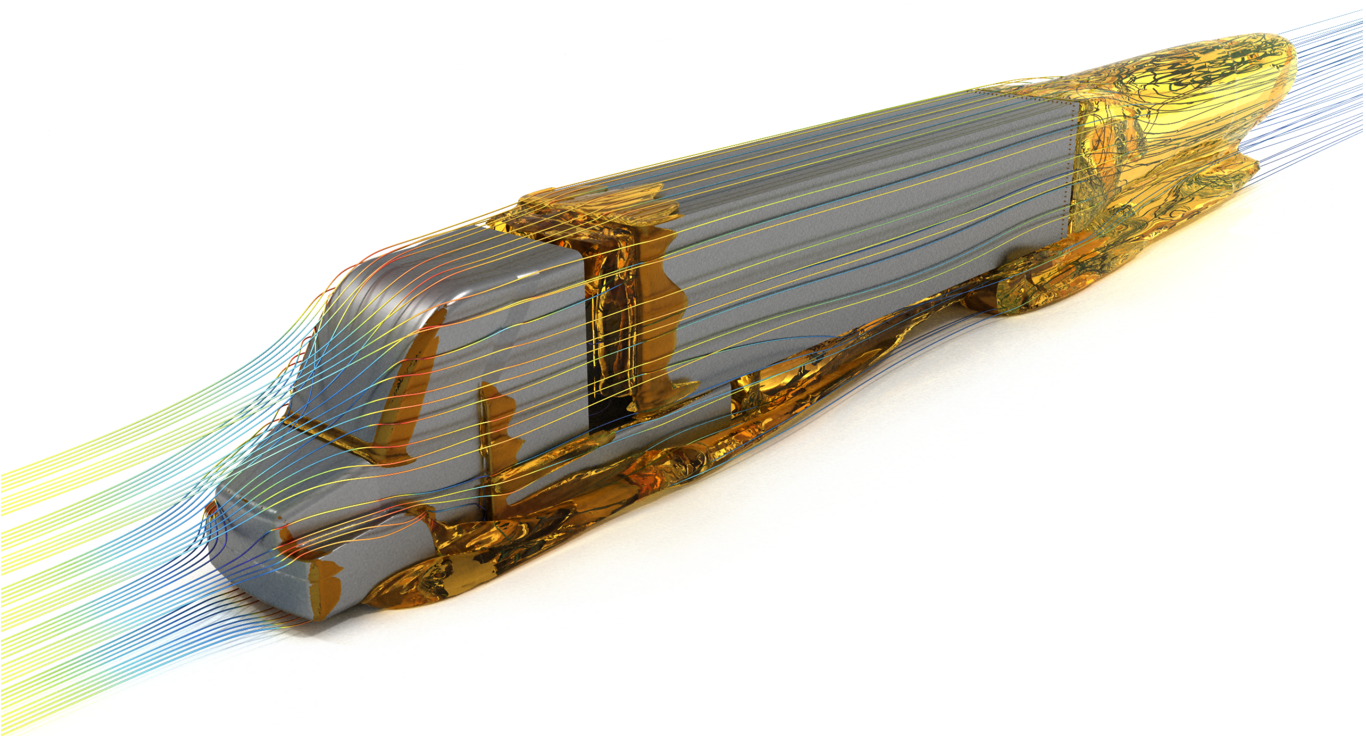

Fig. 1. Streamlines Coloured by Cell Relative Velocity Magnitude (blue=low, red=high). Isosurface of Turbulent Kinetic Energy. Created in Star CCM+

I. Introduction and Background

In the context of heavy vehicles, aerodynamic drag significantly influences fuel consumption and performance, and therefore dramatically impacts emissions and operational costs. It has been shown that aerodynamic drag at highway speeds for Class 8 tractor-trailers contributes to approximately 65% of the vehicle's fuel consumption [2]. These vehicles are known by different terms internationally, including articulated lorries, semi-trailer truck, and so on. For consistency and clarity, the term Class 8 tractor-trailer will be adopted throughout this report.

A tractor-trailer geometrically represents two bluff bodies, one behind the other. These shapes produce complex aerodynamic flow, including large wakes, vortex shedding, flow separation, and gap flow between the tractor cab and the trailer [3]. These structures negatively impact aerodynamic drag, leading to increased fuel consumption and elevated greenhouse gas emissions. In 2018, it was found that the transport sector accounted for 24% of global energy-related CO_2 production, with road freight contributing 29.4% to these transport emissions [4].

The four primary sources of aerodynamic drag for Class 8 tractor-trailers and their corresponding percentage contribution to total drag, as outlined by [5], are the tractor (25%), the gap between the cab and the trailer (22.5%), the undercarriage of the trailer including the wheels, hub, and so on (26.25%), and the rear (base) of the trailer (26.25%).

Various drag-reducing devices have been researched and implemented for these vehicles to reduce the negative impacts of these flow structures, including cab extenders, trailer side skirts, and boat tails mounted to the rear of the trailer. These devices have been proven to work with varying degrees of success [1], [3], [6], [7], but they come with their drawbacks. For example, cab roof deflectors require precise fitment and adjustment depending on the trailer height for optimal effectiveness [8], side skirts are vulnerable to damage [9], and boat tails increase the overhang of the vehicle and are also susceptible to damage [10]. Additionally, these devices' installation complexity and financial cost can be high.

Regulations in certain locations can also prevent the use or limit the size of drag-reducing devices fitted to the rear of heavy vehicles due to legislation restricting their overall length and width. For example, in the United Kingdom, devices which extend over 1 m beyond the rear of the trailer require a red lamp, and retractable devices are recommended to be stowed away in urban environments [11], therefore causing inconvenience to the driver and haulage company. However, recent research displays the possibility of AI-operated flaps [12], which would solve the issue of inconvenience as well as ensuring the flaps are operating at the optimum deflection angle in real-time.

An area lacking research for these vehicles in terms of aerodynamic improvement is bio-inspired solutions, which have proven to be of great success in many engineering designs, such as the Shinkansen bullet train, whose nose cone was developed to mimic that of the Kingfisher bird, and the McLaren P1, whose intake ducts are lined with scales inspired by the sailfish [13]. Whale tubercles, which are large raised bumps on the leading edge of the Humpback whale flipper, have been a popular topic for research into bio-inspired solutions due to their ability to enhance both hydrodynamic and aerodynamic flow characteristics. In industrial contexts, such as wind turbine blades, these tubercles have been shown to increase lift and decrease drag by delaying stall [14], [15]. In the context of automotive aerodynamics, AeroHance pods have been developed to decrease drag, with the shape of the pods being inspired by whale tubercles [16].

The AeroHance pods are typically attached to the rear end of a vehicle on the sides and/or roof using an adhesive pad. They are relatively small, measuring approximately 64 mm in length, 30 mm in width, and 26 mm in height, and are manufactured from lightweight EVA (ethylene-vinyl-acetate). See Figure 23 in Appendix B for details on pod geometry.

Through AeroHance's fuel savings records collected by drivers [17], the pods have been shown to improve the fuel economy of buses by 1.3 %, Class 8 tractor-trailers by up to 2.7 %, and box trucks by up to 11 %. A range of light-duty vehicles have also been analysed, with fuel economy increasing by 2.4-17% when pods are appended.

The following report documents an aerodynamic study of a simplified Class 8 tractor-trailer geometry using Computational Fluid Dynamics (CFD), as well as an investigation into the relationship between drag and the addition of AeroHance pods appended to the trailer, considering various pod configurations. To date, no known studies have used CFD to analyse AeroHance pods attached to a Class 8 tractor-trailer.

II. Methodology

The aim of this research was to identify the relationship between aerodynamic drag and the addition of AeroHance's pods to a generic tractor-trailer geometry using CFD. The methodology comprised of three main objectives, those being: a) CFD validation on a 1/8th scale tractor-trailer geometry using experimental data to ensure the CFD setup physically represents real-world conditions, b) Full-scale tractor-trailer simulations without pods appended to replicate authentic open-road conditions and gather baseline data, c) The study of various pod configurations appended to the tractor-trailer to find the optimum pod arrangement for reducing drag.

For all simulations, STAR-CCM+ from Siemens Digital Industries [18] was utilised to solve the Reynolds Averaged Navier Stokes (RANS) equations, incorporating the effects of viscosity and the modelling of three-dimensional flow.

The first task was to source reputable experimental data from which the CFD setup could be validated upon. Storms et al. [1] conducted experiments within the NASA Ames 7 by 10-foot wind tunnel, whereby a 1/8th scale simplified Class 8 tractor-trailer geometry, the Generic Conventional Model (GCM), was analysed. The wind tunnel case used for validating the CFD was conducted at a yaw angle of $0°$, a Reynolds number of 1.15 million and a Mach number of 0.15. The GCM was mounted in the test section by four vertical posts on the trailer and suspended above the tunnel floor, providing a clearance of 15 mm for the rear wheels and 9 mm for the front wheels due to the cantilevered mounting of the tractor. The boundary layer thickness at the test section entrance was 53 mm, corresponding to a displacement thickness of 15 mm. Please see Figure 21, Appendix A for the model-scale GCM geometry details.

The GCM geometry used within the CFD simulations in this report was obtained from [19], and as stated within the source, was derived from drawings within [1]. Mesh independency studies, a turbulence model sensitivity analysis, and validation of the CFD setup ensured that the simulations were robust and accurately represented the physics within the wind tunnel. The validation points focused on the aerodynamic drag coefficient (C_D) and surface pressure distributions (C_p) along the centreline of the tractor-trailer geometry.

After successful validation, the GCM was scaled to full-size in the second phase, and simulations were run at Reynolds numbers correlating to the general operating conditions of these vehicles. The model-scale setup was closely followed, with minimal changes made to ensure the model remained valid, while incorporating necessary modifications to accurately represent real-world open-road conditions. Simulations were run at four different vehicle velocities, all resembling typical driving speeds of heavy vehicles. Domain studies were also carried out to ensure that the domain size was independent of the results. To allow for scaling effects to be analysed, an additional simulation was performed in which the Reynolds and Mach numbers of the model scale and full-scale configurations matched, thereby ensuring dynamic similarity between the two simulations and enabling direct comparison of the two scales.

In the final phase, the AeroHance pods were appended to the full-scale GCM, and multiple pod configurations were systematically analysed. The pods were mounted to the trailer's roof and/or sides in various arrangements, with each Configuration compared against the baseline simulations without pods appended to analyse their effectiveness in reducing aerodynamic drag. A case study was then conducted to correlate the drag reduction observed with the expected fuel savings.

III. Validation and Verification: Model-Scale Simulations

To match the conditions of the experiment, a trailer width (0.3239 m) based Reynolds number of 1.15 million was computed at a Mach number of 0.15, with a yaw angle of 0° applied for all simulations. The mounting posts supporting the GCM model were included (although not reported in the results, similarly to the experiment), and the GCM was suspended at a height corresponding to the experiment. As mentioned previously, the tractor was positioned at a slight incline within the experiment; this was also considered in the CFD model by rotating the tractor around the y coordinate (cross-stream direction).

The volume mesh was constructed using unstructured trimmed cells, with volumetric refinements applied on surface offsets, the cab-trailer gap, wake regions, and near the wind tunnel walls. Slow growth parameters were used to ensure smooth transitions of cell sizes. Custom surface and curve controls were utilised to refine the mesh in areas where high gradients were expected, such as the leading and trailing edges, wheels, trailer hub, and any other sharp angles or surfaces with high curvature.

The prism layer mesher was employed to accurately model the boundary layer by using high aspect ratio orthogonal prismatic cells, which are aligned with the flow, thereby allowing the high-velocity gradients in this region to be captured. The target number of prismatic cells present over the geometry was between 10 and 18. The first layer heights were chosen such that a low y^+ mesh was present on the tractor, while a high y^+ mesh was used on the trailer, resulting in surface average values of 2 and 55, respectively. This practice follows Siemens guidelines for vehicle aerodynamics [20], allowing cells to be saved in areas where a low y^+ mesh would not provide significant benefits, as will be later proven within this report.

The all y^+ model was applied to ensure the boundary layer is modelled appropriately, allowing the y^+ wall treatment to switch between a wall-function approach in areas where a high y^+ is present, to a low-Reynolds number model in places with a low y^+. Various other settings, such as the minimum thickness percentage, Near Core Layer Aspect Ratio (NCLAR), and gap-fill percentage, were also adjusted to achieve a high-quality prism layer mesh which transitions smoothly to the core, with at least one prism layer present over the whole geometry, even in tight gaps.

As the geometry was symmetric about the centreline, half of the domain was analysed, thereby reducing the computational expense. All figures within this report are mirrored for illustration purposes, with the metrics, cell counts, domain extents, and so on, given relative to the full domain.

A naming convention was adopted for the reporting of metrics due to the amount of data retrieved from the simulations, whereby "F" represents forces, and "M" represents moments. The character immediately following indicates the direction: x (streamwise), y (cross-stream), or z (vertical). The subsequent character(s) specify the component, whereby "p" stands for pressure, "s" stands for shear, and "ps" for the combined pressure and shear. What follows is the coordinate system in which the metric is reported. For example, total drag in the CAD Flow Coordinate System is labelled as "Fxps_CAD_Flow_CS". This coordinate system is described in Figure 6.

The GCM geometry inherently has some time dependent flow, such as within the cab-trailer gap; however, simulations were run in steady-state as the effect of these on the results were deemed to be minimal as noted by the residuals dropping below 1×10^{-3}, the well-converged drag force as displayed in Figure 2, and also as proved by [21], whereby steady-state RANS simulations were conducted on the GCM, achieving excellent correlation with the experimental data. The simulations were run for up to 2500 iterations until the forces achieved a tight convergence criterion of 0.5% over a moving window of the last 400 iterations. The extracted metrics were then averaged across the last 400 recorded values to limit the influence of numerical noise.

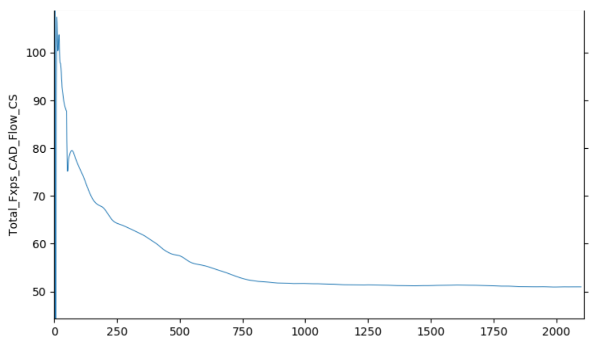

Fig. 2. Example of Convergence: Drag Force vs Iteration Number

The domain extents were placed to match that of the wind tunnel, except for the inlet, which was moved upstream 3.7 m from the original position of the test section entrance to allow the boundary layer to grow to a thickness of 53 mm at a distance of 13.33 cm from the front of the tractor, as documented in the wind tunnel experiments. This distance was calculated using the turbulent boundary layer thickness equation for a smooth flat plate: $\delta/x \cong 0.38/(Re_x)^{1/5}$ [22]. The floor, sides, and top boundaries were modelled as non-slip walls, thereby allowing the growth of a boundary layer as the fluid velocity at the wall is zero. The inlet and outlet boundaries were modelled as a velocity inlet and a zero gradient pressure outlet, respectively.

A. Mesh Independency Study

A study was conducted to ensure the results were independent of the mesh, where the mesh base size was refined by a factor of $\sqrt{2}$ over three simulations in total. The first cell heights were held constant over the three grids to ensure that the y$^+$ values were appropriate for the choice of turbulence modelling and, therefore, sufficiently resolved the near-wall region irrespective of the grid resolutions used within the study. The metric analysed within this study was the drag coefficient, which was one of the key measures used to validate the simulations with the wind tunnel data, defined by:

$$C_D = \frac{D}{0.5\rho U^2 A} \tag{1}$$

where D is the drag force, ρ is the fluid density, U is the freestream velocity, and A is the frontal area of the GCM (0.154 m^2). Within the experimental data, the C_D value obtained was 0.406 [23]. The turbulence model used within this study was the Menter SST K-ω [24], with the a_1 and Realizability Coefficients set to 1.0 and 1.2, respectively, as discussed in the subsequent section of this report. As shown in Figure 3, C_D exhibits monotonic convergence, noted by the convergence ratio $0 \leq CR < 1$, defined as $CR = \epsilon_{21}/\epsilon_{32}$, where ϵ_{21} and ϵ_{32} represent the differences in C_D between consecutive grids, i.e., $\epsilon_{21} = C_{D_{Grid2}} - C_{D_{Grid1}}$.

TABLE I
MESH STUDY

Grid #	Base Size (m)	Cell Count	CFD C_D	AR	ΔC_D	GCI	Error to $f.exact$
1	0.297	20.68e6	0.415		2.11%	0.96%	0.32%
2	0.420	11.75e6	0.417	0.994	2.74%	2.83%	0.94%
3	0.594	6.89e6	0.425		4.58%	N/A	N/A

$^{\Delta C_D}$ Comparative difference between the experiment and CFD results.
$^{Error\ to\ f.exact}$ Percentage error relative to the extrapolated solution.

The Asymptotic Range (AR) results in a value of 0.994, thereby suggesting that the solution is close to converging in the asymptotic range as it tends to one. The Grid Convergence Index (GCI) informs us of the spatial uncertainty and was calculated using a conservative factor of safety of 3, with grid 1 obtaining a GCI of 0.96%, and an error of 0.32% to the extrapolated solution at an infinite mesh size. The observed characteristics of the mesh study, therefore, display that the solution is well converged, with grid 1 obtaining a low level of uncertainty - thus, the mesh was taken forward for subsequent simulations.

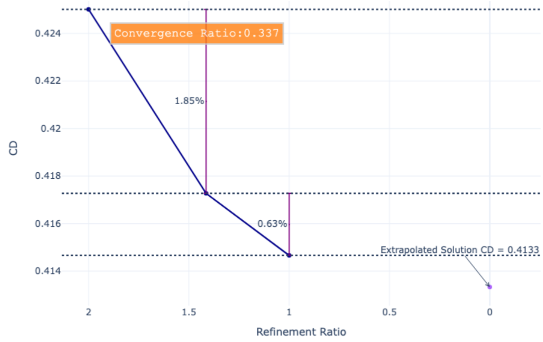

Fig. 3. Mesh Study Convergence: C_D vs Refinement Ratio

To calculate the iterative error, the method as described within [25] was utilised:

$$\varepsilon^n_{\text{iter},i} \cong \frac{(\phi_i^{n+1} - \phi_i^n)}{\lambda_i - 1} \tag{2}$$

$$\lambda_i \cong \frac{\|\phi_i^{n+1} - \phi_i^n\|}{\|\phi_i^n - \phi_i^{n-1}\|} \tag{3}$$

$$\delta_{\text{iter}} \cong \frac{\|\varepsilon^n_{\text{iter},i}\|}{\lambda_{\text{ave}} - 1} \tag{4}$$

where $\varepsilon^n_{\text{iter},i}$ is the iteration error, n is the iteration number, ϕ is the physical quantity of interest (which in this case was C_D), and δ_{iter} is the iteration uncertainty.

The resulting estimated iterative error was 0.005% with an iterative uncertainty of 0.058%, using the last 400 iterations to calculate λ_{Ave}. The iterative uncertainty was therefore deemed negligible as it is over one order of magnitude smaller than that of the grid uncertainty.

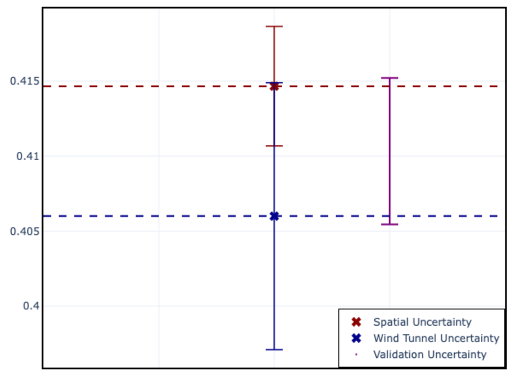

Fig. 4. Uncertainties

Figure 4 displays the spatial uncertainty of the CFD ($U_{Grid} = 0.96\%$), the uncertainty of the experimental data ($U_{WT} = 2.22\%$) as noted within Table 1 of [1], and the validation uncertainty, all of which are in relation to C_D. To determine the validity of the study, the comparative error is compared against the validation uncertainty, defined as $U_V = \sqrt{U^2_{WT} + U^2_{Grid}}$ [26]. The setup is valid as the comparative error between the wind tunnel data and the CFD results (2.11%) is less than U_V (2.37%).

B. Turbulence Modelling

The turbulence intensity of the simulations was selected to match that of the wind tunnel experiments (0.25%). No transition models were used, thus assuming a fully turbulent boundary layer. Two turbulence models were tested, those being the Menter SST K-ω, and the Realizable K-ϵ Two-Layer (RKE 2L), both of which allow the use of the all y$^+$ model mentioned in previous sections of this report.

Following STAR-CCM+ best practice guidelines for vehicle aerodynamics [20], the a_1 and realizability coefficient (C_T) within the K-ω model were changed to 1 and 1.2, respectively. As reported in [27], the a_1 default value of 0.31, as well as the default of 0.6 for C_T, tends to over-predict flow separation. In relation to this current research, [27] also studied the flow separation over a 2D hump (geometrically similar to a pod), where this over-prediction of flow separation could be seen when the default values were adopted, whereby the computed flow separation deviated from the experimental studies. However, the results yielded a much better correlation when the a_1 coefficient was changed to the recommended value.

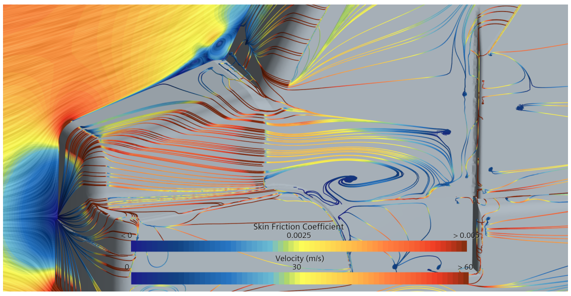

(a) Default K-ω Settings

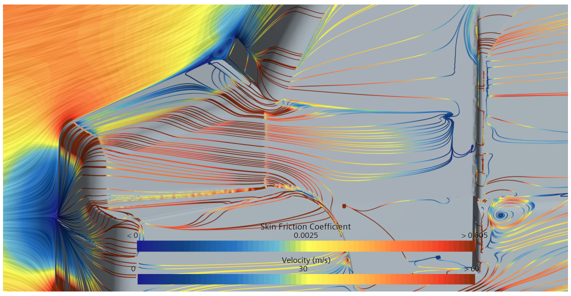

(b) Modified K-ω Settings (a_1 = 1, C_T = 1.2)

Fig. 5. Constrained Streamlines Displaying C_f, and LIC on an XZ Centreline Plane displaying velocity

The modified coefficients were compared with the default values by running an additional simulation, in which the a_1 and C_T values were changed from the recommended values to their defaults. As expected, the default values of 0.31 for a_1 and 0.6 for C_T resulted in more flow separation over the tractor, as can be seen when comparing Figures 5a & 5b. When looking at the Line Integral Convolution (LIC: an advanced post-processing technique to visualise the flow field) displayer in Figure 5a, a larger recirculation bubble can be seen at the base of the windscreen, with multiple vortices formed. More flow separation can also be observed on the side of the tractor, as denoted by the constrained streamlines in areas where the skin friction coefficient (C_f) tends to a value of zero, and the streamlines take a chaotic form. In both cases, there is almost no flow separation over the trailer, except for a minimal amount on the roof at the leading edge.

The findings of the turbulence study are presented in Table II. In the context of the K-ω model, the case employing the default coefficient settings yielded a higher total drag over the tractor, as expected, due to increased flow separation. However, the drag on the trailer reduced, the reasons for which remain unclear having not been explored within this study. The resulting total drag of the simulation was 0.54% lower than that of the case with recommended coefficient settings, meaning that the default values obtained a slightly lower comparative error when measured against the experimental data. However, when comparing the convergence of the two simulations, the recommended coefficients yielded a much more stable solution, whereas the default values displayed substantially worse convergence characteristics, as noted by the greater erratic behaviour of the forces in the iterative history and the higher residual values. This follows findings within [27], whereby the recommended values stabilised the solution.

The RKE 2L model underpredicted the drag with a much higher relative error when compared to the experiment. Consequently, the K-ω model with the recommended coefficient values was selected for subsequent sections of this report. While no validation results are available to confirm the usage of the adjusted coefficients in this particular case, the selection aligns with recommendations from Siemens [20], the findings within other cases [27], and observations made within this report in terms of stability and convergence.

TABLE II
TURBULENCE MODEL STUDY

Turbulence Model	**Tractor Fxps**	**Trailer Fxps**	**CFD** C_D	**WT** C_D	ΔC_D
K-ω, a_1=0.31, C_T=0.6	38.29	63.21	0.412		1.56%
K-ω, a_1=1, C_T=1.2	36.85	65.22	0.415	0.406	2.11%
RKE 2L	37.20	57.99	0.387		4.87%

C. Pressure Coefficients

A single point is usually insufficient for validating a simulation [28], thus the pressure coefficient (C_p) along the GCM centreline was also compared to the experiment, defined as:

$$C_p = \frac{p - p_{\text{ref}}}{\frac{1}{2}\,\rho U^2} \tag{5}$$

where p is the local static pressure, and p_{ref} is the reference static pressure measured at a wall probe point, corresponding to the exact location used in the wind tunnel experiment, as described in Figure 22, Appendix A.

Figures 6a & 6b display the centreline pressure distributions of the tractor and trailer, respectively. The experimental data presented here was extracted from [23]. The correlation between the experimental and CFD data is very good, with only minor deviations around the rear of the trailer, and the base of the tractor windscreen where a sharp step is present, leading to separation and some unsteady flow. It should be noted that the previously discussed simulation utilising the default a_1 and C_T values obtained a very similar level of correlation in the Cp plots. Some changes to the geometry of the tractor's roof were necessary after initial findings revealed a notable pressure deviation in this area due to a step in the roof, which was initially present in the CAD file and does not exist in the GCM geometry used within the experiments. After the changes were made to the geometry to match the GCM model, a much better correlation was observed.

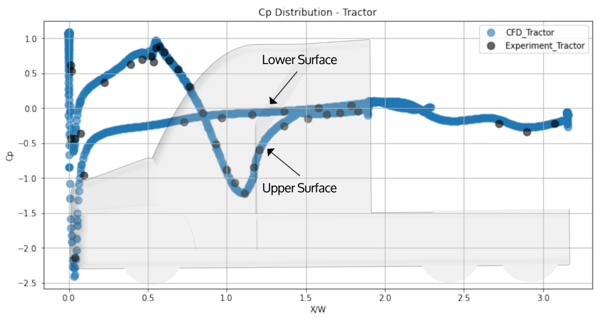

(a) Tractor Centreline Pressure Distribution vs Horizontal Coordinate

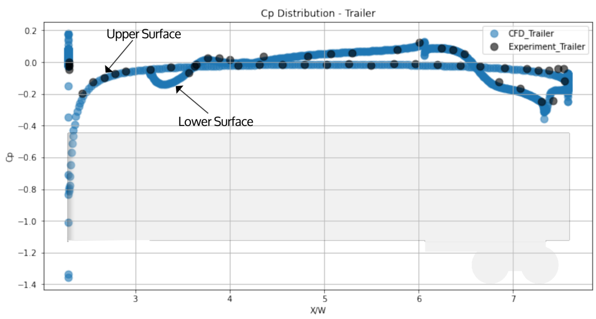

(b) Trailer Centreline Pressure Distribution vs Horizontal Coordinate

In conclusion for the present section of this report, it was demonstrated that the setup obtained a very low comparative error in both the C_D and the C_p results for the chosen grid 1 resolution. The model also displayed sufficiently good characteristics in the verification studies, with a low uncertainty of 0.96% in the grid and negligible iteration uncertainty.

IV. Full-Scale Simulations

The GCM geometry was scaled up to full size and used for the subsequent sections of this report. A trailer width-based (2.59 m) Reynolds number of 5.5 million was computed at a velocity of 26.8 m/s.

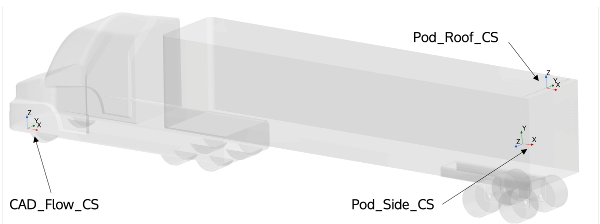

Fig. 6. Coordinate Systems Used Within Full-scale Simulations.

Figure 6 identifies the coordinate systems used within the full-scale simulations. The CFD forces and moments are reported within the CAD_Flow_CS, which has the origin at the front of the tractor, with the x-axis pointing downstream, the y-axis to the right when sat in the vehicle, and the z-axis pointing upwards. The origin of this coordinate system moves with the translation of the vehicle, which is relevant only for setting the initial ground clearance as the simulations were run with 0 degrees of freedom.

A local coordinate system was created for each pod, with their origins and orientations defined according to the desired pod positions and angles of attack (AoA). A coordinate transform was then applied to position the pods based on these local reference frames. The pod coordinate systems are therefore aligned with the pods, with the z-axis perpendicular to the trailer surface on which they are appended, and the x-axis pointing toward the trailing edge of the pod. One pod coordinate system is displayed per trailer surface for which the pods are appended to in Figure 6 for illustration purposes only.

A. Domain and Mesh

To retain as much similarity as possible to the validated model-scale setup, the mesh base size was scaled by the same factor used to scale up the geometry. The prism layer settings were adjusted to account for the new Reynolds number and boundary layer thickness. Volumetric and surface mesh controls were added to the pods and surrounding areas to capture the flow phenomena accurately. The mounting posts were removed, and the GCM was lowered onto the floor, with small blocks added under the wheels to improve the mesh at the intersection between the tyres and the floor. Please see Figure 24 in Appendix B for an example of the mesh used within full-scale simulations.

The wind tunnel walls were removed, with a symmetry boundary condition applied to the sides and top, and a moving ground plane with a tangential velocity set to the vehicle speed was employed for the floor boundary.

TABLE III
Domain Study

Downstream	Upstream	W	H	Blockage	C_D	ΔC_D
$35G$	$20G$	$20G$	$10G$	0.48%	0.399	0.34%
$28G$	$16G$	$16G$	$8G$	0.75%	0.400	0.96%
$22G$	$13G$	$13G$	$6G$	1.23%	0.404	1.16%
$18G$	$10G$	$10G$	$5G$	1.91%	0.409	N/A

A domain study was carried out to ensure that the results were independent of the domain size. Four domain sizes were analysed, as listed in Table III. To ensure appropriate domain extents, a characteristic length G was defined as $G = \sqrt{W \times H}$, where W and H represent the width and height of the vehicle, respectively. The domain boundaries were then placed at multiples of G.

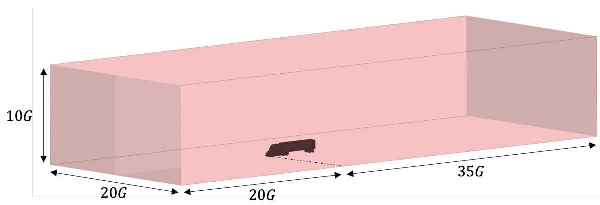

Fig. 7. Final Domain Extents

As noted in Table III, the parameter ΔC_D, which is the difference in C_D between consecutive simulations, identifies that the solution reaches convergence as the domain sizes increase and the blockage ratio reduces. The largest domain demonstrated near independence of results on the domain size, with a small ΔC_D value of 0.34%, and a resultant blockage ratio of below 0.5%, thereby following recommendations within [29]. Consequently, this domain size was taken forward for the subsequent simulations.

B. Boundary Layer Transition Modelling

To ensure that the flow could be assumed fully turbulent, a study was carried out to determine the extent of laminar flow present on the GCM. Although this was not done within the model-scale validation as it was deemed unnecessary due to the good validation results, the flow regime changed in full-scale simulations. The Gamma ReTheta transition (GRT) model [30] was used to predict the onset of transition in the boundary layer. Cross-flow terms were activated to account for cross-flow instabilities and the onset of transition due to destabilisation of the boundary layer from velocity components acting across the primary flow direction. As with all simulations, the roughness height was set to represent a general value for automotive paint of (1.03×10^{-6} m) [31].

The simulation setup used within this study was Configuration 1 (pods appended to the GCM), as described in later sections of this report, and Table VI (see Appendix B). As the transition model requires a very high-quality mesh within the boundary layer to accurately predict transition, the previously adopted high y^+ mesh over the trailer was adapted to achieve a y^+ surface average value of approximately 2. Two simulations were run to isolate the effects of turning the transition model on, with the mentioned changes performed systematically, thereby allowing for a fair comparison.

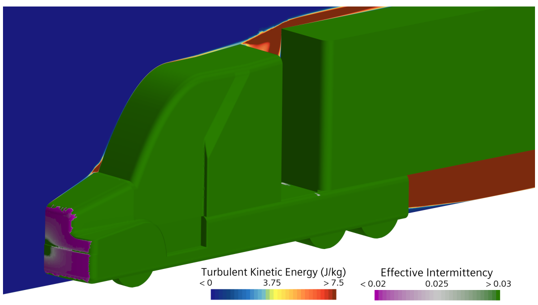

Fig. 8. GRT Model On: XZ Centreline Plane Displaying Turbulent Kinetic Energy. GCM Surface Scalar Displaying Effective Intermittency.

Figure 8 displays a scene within the simulation in which the GRT model is turned on. The surface of the GCM is coloured by intermittency, whereby purple represents a laminar boundary layer (a value of 0.02), and green highlights a fully turbulent regime (a value of 0.03) [32]. When examining the front face of the tractor, a turbulent boundary layer region can be identified around the stagnation point, quickly changing to a laminar regime. This then transitions back to a turbulent boundary layer over the bonnet of the GCM at an Re_x number of approximately 5×10^5. The remaining areas of geometry show little to no laminar regimes. Over the trailer, there is no laminar boundary layer at all, and this appears to be caused by a small recirculating separation region at the leading edge, as well as turbulent flow coming from the gap between the cab and the trailer, flowing over and around the sides of the trailer and thereby setting the initial condition for the boundary layer to be of a turbulent regime, as highlighted in the XZ centreline plane displaying turbulent kinetic energy in Figure 8.

TABLE IV
TRANSITION MODEL STUDY

GRT Model	Mesh Type	Tractor Fxps	Trailer Fxps	CFD C_D	ΔC_D
Off	Low y^+ Tractor High y^+ Trailer	671	1089	0.391	N/A
Off	All Low y^+	674	1095	0.393	0.49%
On	All Low y^+	672	1098	0.394	0.59%

In conclusion, the resulting run time of the simulation with the GRT model activated (and therefore also adopting a finer mesh) was 125% longer than that of the standard Configuration 1 setup. The large increase in computational time resulted from the refined mesh containing 48 million cells (compared to 27 million for the standard setup), and the additional physics processes from the GRT transition model. Thus, the technically more physically accurate simulation was not worth the extra computational expense due to the minimal amount of laminar flow present, and the very small differences in results (0.1% in C_D) , as displayed in Table IV.

When comparing the effects of y^+ over the trailer, the small difference in C_D of 0.49% between the standard Configuration 1 simulation which employed a high y^+ mesh over the trailer, and the simulation with an all low y^+ mesh (with GRT model turned off), thereby supports the previously mentioned recommendations from Siemens [20] to utilise a low y+ mesh over the tractor, and high y+ mesh over the trailer. As the difference in results is slight, and the cell count almost doubles, it is clear that implementing a low y^+ mesh on the trailer leads to an unnecessary increase in cell count. Due to the findings of this study, the previously adopted methods from Configuration 1 were carried forward.

C. Results

1) Comparison of Model-Scale & Full-Scale Simulations: In the wind tunnel experiments, the reported frontal area appeared to exclude the wheels; thus, this frontal area was also used for the model-scale simulations. However, for the full-scale simulations, the frontal area, as calculated directly from the CFD software (including wheels), was used due to anticipated changes in the frontal area from the appending of the pods. To facilitate a direct comparison between model-scale and full-scale simulations, within this section only, the full-scale frontal area excluding the wheels was used.

When comparing the full-scale simulation conducted at a Reynolds number of 5.5 million (Configuration 0 ID:003, no pods appended as discussed later in this report) to the model-scale simulation, a decrease of 1.11% in C_D was observed in the former. To analyse the effects of scaling up the geometry on these results, an additional simulation was performed to achieve dynamic similarity by matching the Reynolds and Mach numbers of the full-scale setup to those of the model-scale simulations. This revealed a decrease of 0.48% in C_D

within the full-scale simulation when compared to the model-scale case, suggesting that the Reynolds and Mach number effects account for a 0.63% decrease in C_D within the full-scale setup conducted at a Reynolds number of 5.5 million.

When considering the modifications made to the full-scale setup, such as the moving ground plane, removal of the model support posts and wind tunnel walls (and so lower blockage ratio due to the increased domain extents), and the lowering of the geometry so that the tyres intersect the floor, the decrease in C_D was anticipated, as detailed in the following factors below:

- Decreasing the ground clearance of bluff bodies results in a reduction of drag, as observed by Barlow et al. [33].
- As found in the domain study, decreasing the blockage ratio results in less drag, consistent with findings in [7]. A blockage of 2.4% was present in the model-scale simulations, whilst the full-scale simulations had a blockage of 0.48%.
- Although the mounting posts in the model-scale simulations were not included in any reports, the wake structures created by their presence most likely caused additional drag on the model. Therefore, removing them entirely from the simulation would cause a credible decrease in drag.

The above arguments therefore explain the most plausible causes for the discrepancies seen in C_D between the full-scale and model-scale simulations in which dynamic similarity was achieved, and so the contribution of scaling effects is presumed to be minimal.

2) Design of Experiments: Table VI (see Appendix B), details the full–scale design of experiments, including the pod orientations for multiple configurations. The pod placement optimisation parameters - AoA, pod spacing, horizontal positioning along the trailer, and their location on the trailer (either the sides, roof, or both) - were all chosen due to their expected influence on how well the pods will perform in terms of drag reduction. The design of experiments was also set up in an attempt to find the boundaries of the design space, with the exception of pod AoA due to the vast number of possible orientations. Please see Figure 9 for a description of the specified parameters of the study.

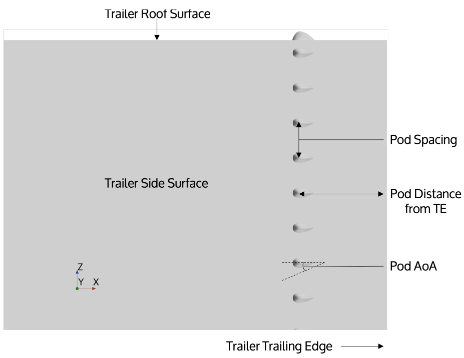

Fig. 9. Configuration Parameter Description

All simulations with pods appended were run at a vehicle velocity of 26.8 m/s to represent general highway speeds, unless stated otherwise.

3) Configuration 0: This Configuration is the baseline setup without pods appended, which is used to compare the results of the various pod configurations. The simulations were run at four different velocities, selected to represent typical highway and interstate speeds as described within [34], as well as average commercial vehicle operating speeds obtained from multiple haulage companies operating Class 8 tractor-trailers [35].

The flow around the body is quite complex; multiple large vortices are formed around the geometry, two of which are formed under the trailer due to mixing the free stream flow and the slower underbody flow. These vortices propagate downstream along the lower edge of the trailer and extend into the wake. Vortices are also formed on the upper corners of the trailer where the roof and side surfaces meet, and again extend downstream into the wake. The longitudinal vortices within the wake likely increase the entrainment of fluid, thus the flow detaching from the trailer curls up aggressively into the wake region, forming strong vortices which directly interact with the base, therefore decreasing base pressure and increasing the drag. The pressure drag dominates, making up 88.6% of the total drag force at a vehicle velocity of 26.8 m/s.

4) Configuration 1 - Baseline Pod Configuration: This section details the baseline pods appended setup, from which all other pod configurations are primarily based upon. Figure 10 displays the total drag build-up by surface of Configurations 0 & 1. Please refer to Figures 25 & 26 (see Appendix B) for details on surface names, and a visual representation of the local drag, respectively.

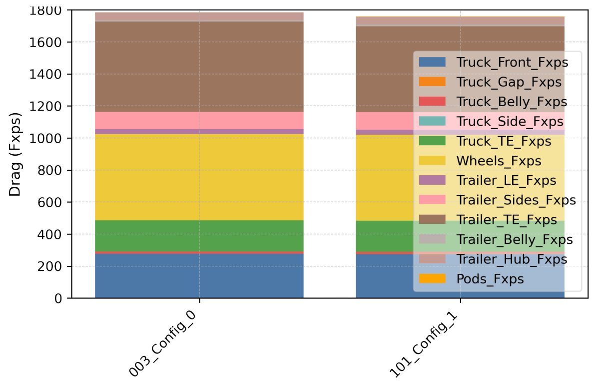

Fig. 10. Configurations 0 (ID:003) & 1: Total Drag Build-up by Surface

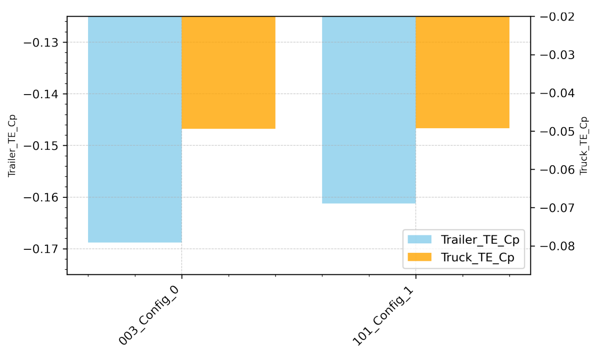

Fig. 11. Configurations 0 (ID:003) & 1: Tractor and Trailer Base Pressure C_p

In Configuration 0 ID:303, the bulk of the drag comes from the Trailer base and the wheels, contributing to approximately 31% and 30% to the total drag of the vehicle, respectively, thereby following closely with findings within [5]. Almost all of the drag reduction in Configuration 1 is from the decrease in trailer base drag, as a result of the increase in trailer base pressure, as shown in Figure 11. Little change in the tractor base pressure was observed when pods were appended.

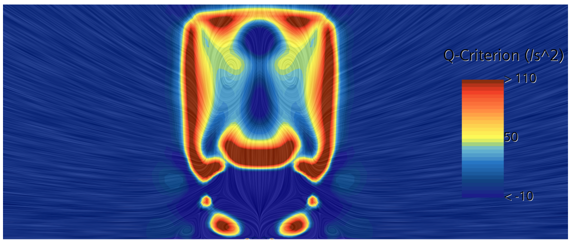

(a) Config_0 - ID:003 (No Pods)

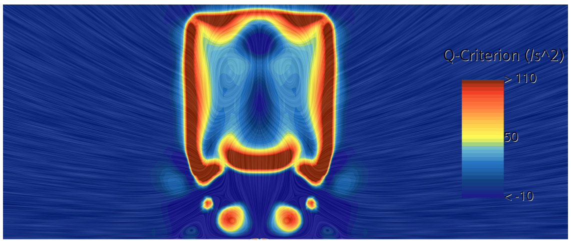

(b) Config_1 - ID:001 (Pods Appended)

Fig. 12. YZ Plane Section at X = 21m (1.35m Downstream of Trailer TE), Displaying LIC with Velocity as Vector Field, Coloured by Q Criterion

Figure 12 displays an LIC on a YZ plane positioned approximately 1.35 m downstream of the trailer base, with the vector field being $|U|$. The scalar is coloured by the Q criterion, defined by $Q = 1/2(||\Omega||^2 - ||S||^2)$ [36], where Ω is the spin tensor, and S is the strain-rate tensor. It can be noted that when Q is positive, the flow is vorticity dominated, whilst a negative value of Q represents that the flow is strain dominated. The stream-wise vortices within the wake are reduced in strength, thus reducing entrainment and the aggressive curl of flow into the wake. The shear layer is also more dominated by vortical structures in Configuration 1.

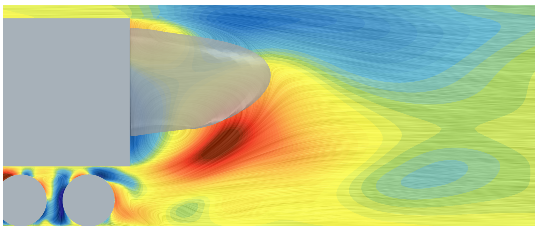

(a) Config_0 - ID:003 (No Pods)

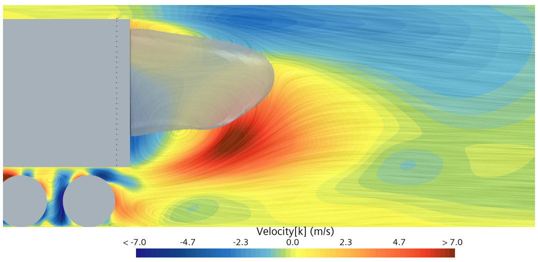

(b) Config_1 - ID:001 (Pods Appended)

Fig. 13. Isosurface on Velocity[i] = 0. LIC at Y = -0.225 * Trailer Width with Velocity as Vector Field, Coloured by Velocity[k]

Figure 13 displays an isosurface of velocity [i] with an isovalue of 0 to highlight the recirculation bubble, and an XZ plane positioned at Y = -0.225 * trailer width, displaying an LIC with velocity as the vector field, and velocity [k] as the coloured scalar. As the scalar field is coloured by the vertical velocity component, we can see areas where the flow has high up-wash (red) and high downwash (blue). With pods appended (Figure 13b), the flow can extend further downstream before curling up into the wake region. The vortex cores and the recirculation bubble also shift slightly further downstream and away from the trailer base in the case of pods appended, which as observed by [37], can be attributed to a decrease in drag. As also found by [38], the reduction in velocity of the vortices which directly interact with the base of the trailer is also reduced, thus attributing to an increase in base pressure. The volume average turbulent kinetic energy within the recirculation bubble also decreased when pods were appended, from a value of 14.82 to 13.52 J/kg.

5) Configuration 2 - Location of Pods: Configuration 2 investigated the effects of changing the location of the pods, either only on the roof, or only on the sides of the trailer. As can be seen from Figure 14, the best layout is one which employs pods on both the sides and roof of the trailer as present in Configuration 1, as the reductions in drag are not as significant when comparing sides only (ID:201), and roof only (ID:202) configurations. The roof pods appear to have less of an effect on the reduction of drag than the pods on the sides, the cause of which may be as simple as the fact there are significantly fewer pods present on the geometry in a roof-only configuration, and so the beneficial modification of structures in the wake is less significant.

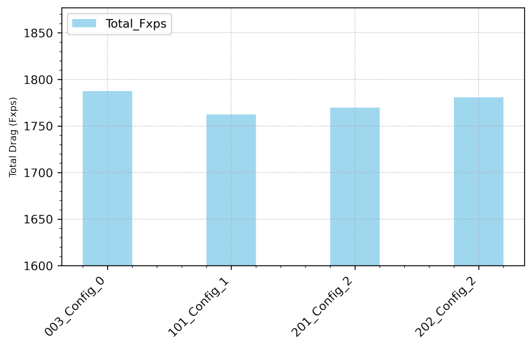

Fig. 14. Configurations 0 - 3: Drag

Comparing the configurations begins to reveal a clear correlation between drag and how aggressively the flow curls into the wake region after separating from the trailer's trailing edge. As previously mentioned, Configuration 1 allows the flow to extend further downstream before being drawn into the wake. In Configuration 2 (ID:201), this distance is reduced, and it is further decreased in Configuration 2 (ID:202). Consequently, the drag increases progressively with the strength and immediacy of this flow entrainment into the wake region.

6) Configuration 3 - Horizontal Position of Pods: A study was conducted to analyse the effect of moving the pods along the horizontal coordinate of the trailer, from the trailing edge to the leading edge. Within Figure 15, there is a clear trend by which moving the pods towards the trailing edge of the trailer results in a more significant reduction in drag, with the optimum position being ID:305. Within [39], D-shaped objects of various sizes were appended to a bluff body at multiple distances from the base. Although it was found that the objects resulted in a drag increase, the magnitude of this depended upon their proximity to the base of the body, with obstacles closer to the trailing edge producing a smaller drag increase. This was attributed to the merging of the obstacle wakes with the wake of the bluff body, as opposed to entirely isolated wakes, which was present when objects were more distant from the base. Therefore, this wake interaction may partially explain why the pods perform better when placed closer to the trailer's trailing edge. Moving the pods to either the centre or the leading edge of the trailer resulted in the effectiveness of the pods diminishing significantly, with ID:303 being the only configuration tested which resulted in a slightly higher drag force when compared to Configuration 0.

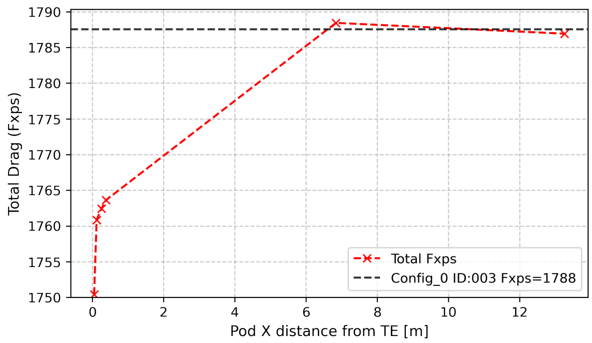

Fig. 15. Configurations 1 & 3: Drag vs Pod x-Distance from Trailer Trailing Edge

Within Figure 16, an isosurface was created to isolate the wake, thereby allowing for analysis in this region by setting the isosurface to act on the velocity deficit defined as: $(U_\infty - |U|)/U_\infty$. As the velocity deficit tends to 1, the momentum loss in the fluid is more significant when compared to U_∞, with a value of 0 representing free stream velocity. The isovalue was set to 0.25, representing the core of the free shear layer, which was identified by high vorticity in the outer wake of the trailer. The flow in the figures is from left to right. The distance to wake reattachment is shorter by 2.12% when the pods are appended, and the pressure in the free shear layer is somewhat higher, especially in the near wake. It was also observed that the recirculation bubble stretched further away from the base by 4.5%.

(a) Config_0 - ID:003 (No Pods)

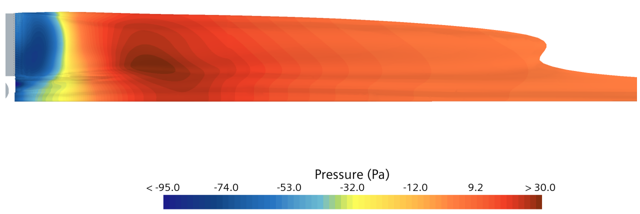

(b) Config_3 - ID:305 (Pods Appended)

Fig. 16. Isosurface Acting on Velocity Deficit = 0.25, Coloured by Pressure

When analysing the wake in ID:303 (pods positioned at the trailer midpoint), the positive effects as seen in Configuration 1, Figure 13b are no longer present, and instead the flow curls up into the wake region aggressively, as seen in Figure 17b, thus leading to a decrease in base pressure. The wake length to reattachment was also approximately 1.8% further downstream than that of the no pods Configuration. The above reasons therefore are attributed to an increase in drag.

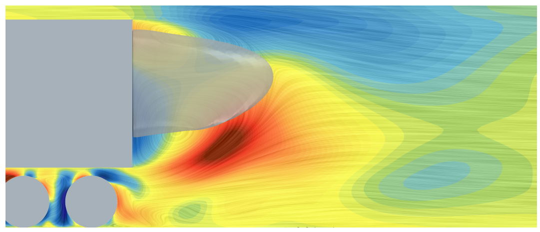

(a) Config_0 - ID:003 (No Pods)

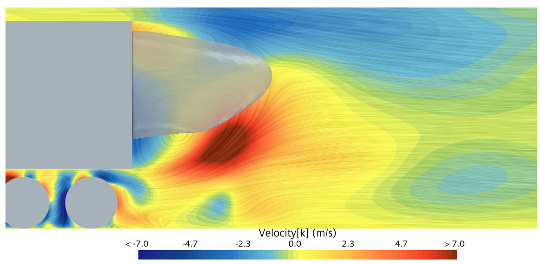

(b) Config_3 - ID:303 (Pods Appended)

Fig. 17. Isosurface on Velocity[i] = 0. LIC at Y = -0.225 * Trailer Width with Velocity as Vector Field, Coloured by Velocity[k]

7) Configuration 4 - Pod Spacing: The pod spacing was defined as the distance between pod centres in the y-axis of the corresponding pod coordinate system. Increasing the spacing of the pods therefore reduced the number of pods present on the geometry. Within Configuration 1 (before the domain was halved), there were 25 pods present on the roof and 29 on each side. By increasing the spacing from 0.1016 m to 0.1270 m (Config_4 ID:401), there were 21 pods on the roof and 23 on each side. And finally, a spacing of 0.1524 m (Config_4 ID:402), resulted in 17 pods present on the roof, and 19 on each side.

Figure 18 displays the effect of the pod spacing on the total drag, where Configuration 1 was added to the graph for completeness. In a similar fashion to findings within Configuration 2, it appears that reducing the amount of pods present on the geometry leads to a reduction of their effectiveness as the base pressure decreases. The best spacing analysed was therefore one which employed a distance of 0.1016 m between the pod centres.

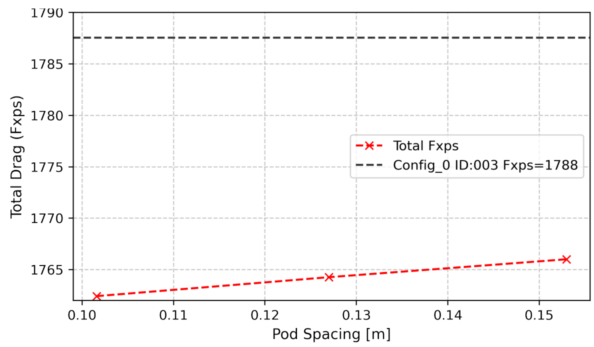

Fig. 18. Configurations 1 & 4: Drag vs Pod Spacing (Y in Pod_*_CS)

8) Configuration 5 - Pod Angle of Attack: Within Configuration 5, the effect of changing the AoA of the pods (as defined by the rotation of the pods around the z-axis of the corresponding pod coordinate system) was analysed. Six different variations were tested, with the effect on the total drag being presented in Figure 19. All variations decrease the drag when compared to Configuration 0, although none of them exceed the reduction in drag seen when the pods are oriented at an AoA of 0° (Configuration 1), with the exception of ID:505. However, the difference in drag reduction between Configuration 1 and ID:505 is slight, as seen in Table V.

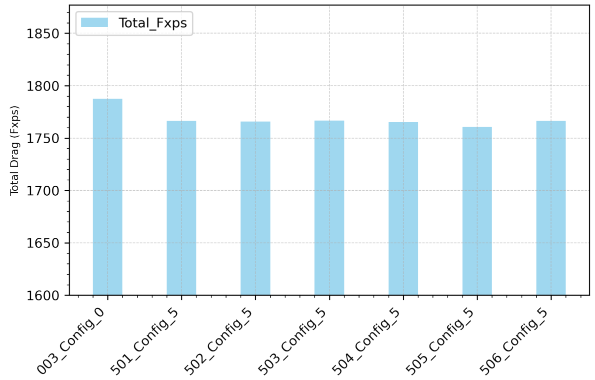

Fig. 19. Configurations 0 & 5: Drag & Lift Coefficients

Common to previous configurations, the recirculation bubble for ID:505 stretched downstream away from the trailer's trailing edge, extending 15 cm more than Configuration 0. The base pressure increased slightly when compared to Configuration 1, thereby attributing to a decrease in drag.

9) Discussion & Configuration 3 Velocity Study: The findings of the pod placement optimisation study indicate that the best Configuration is one which employs pods on both the roof and side surfaces, located as close to the trailer's trailing edge as possible, with a spacing of 0.1016 m between pods. It appears that applying a pod AoA generally decreases the effectiveness of the pods, except in the case of ID:505, whereby an AoA of 5° was used for the pods down the side of the trailer. However, the improvement was minimal, thus the general recommendation remains to utilise pods with an AoA of 0 °.

To study the effectiveness of the pods at varying speeds, simulations were conducted using the best performing Configuration in terms of reduction in drag force, Configuration 3 ID:305, as seen in Table V. It should be noted that the addition of pods and the parameters defining each Configuration result in varying frontal areas. Therefore, direct comparisons using C_D is not an accurate measure of aerodynamic performance. To overcome this, the product of the drag coefficient and frontal area can be used (C_DA). By comparing this metric, the results can be better graphically represented as an extensive range of values is avoided across the velocity range (as would be apparent if drag force was to be compared), and the aerodynamic efficiency can still be accurately compared between pods vs no pods, irrespective of the frontal area.

The setup of these simulations mirrored that of ID:305 but were run at the same four velocities as the simulations in the Configuration 0 group. Figure 20 displays a plot of C_DA vs velocity for Config_3_VelStudy, and Configuration 0 for comparison. The drag is reduced for all speeds tested, with the highest reduction in drag apparent at a velocity of 31.29 m/s. It is also clear that the effectiveness of the pods grows as the velocity increases.

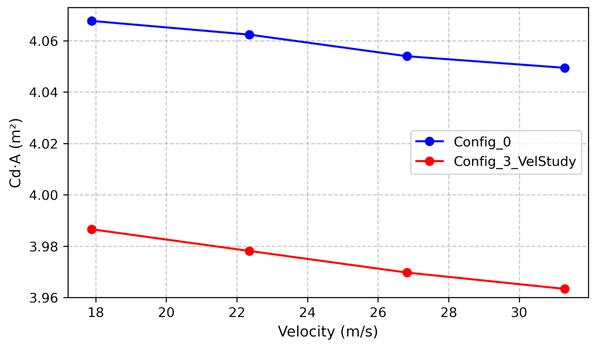

Fig. 20. (Config_0 & Config_3_VelStudy): C_DA vs Vehicle Velocity (m/s)

TABLE V
FULL-SCALE DESIGN OF EXPERIMENTS RESULTS

Config	ID	Total Fxps (N)	$\Delta Fxps$	C_D	C_DA (m^2)
Config_0 (No Pods)	001	797	N/A	0.400	4.068
	002	1244	N/A	0.399	4.062
	003	1788	N/A	0.399	4.054
	004	2430	N/A	0.398	4.049
Config_1 (Baseline Pods)	101	1762	1.41%	0.391	3.997
Config_2 (Trailer Surface)	201	1770	0.99%	0.394	4.014
	202	1781	0.38%	0.397	4.038
Config_3 (Lateral Position)	301	1761	1.49%	0.391	3.993
	302	1764	1.34%	0.392	4.000
	303	1788	-0.05%	0.397	4.056
	304	1787	0.03%	0.397	4.053
	305	**1750**	**2.08%**	**0.389**	**3.970**
Config_4 (Axial Spacing)	401	1764	1.30%	0.392	4.001
	402	1766	1.20%	0.393	4.005
Config_5 (Pod AoA)	501	1766	1.18%	0.392	4.006
	502	1766	1.22%	0.392	4.004
	503	1767	1.17%	0.392	4.007
	504	1765	1.26%	0.392	4.003
	505	1760	1.52%	0.391	3.993
	506	1766	1.19%	0.392	4.006
Config_3_VelStudy (ID:305 Velocity Study)	701	781	1.99%	0.390	3.987
	702	1218	2.07%	0.390	3.978
	703[a]	1750	2.08%	0.389	3.970
	704	2379	2.12%	0.388	3.963

[a] : (Config_3_VelStudy ID:703) = (Config_3 ID:505), duplicated for clarity.
$^{\Delta Fxps}$: $Fxps$ decrease as compared to the no pods comparative case.

D. Expected Fuel Savings: Case Study

Utilising the best performing Configuration, a study was conducted to investigate how the resulting drag reduction seen could translate into a decrease in fuel consumption, reduced CO_2 production, and financial savings. As a case study, a fleet of 10 Class 8 tractor-trailers was considered, each making a stop approximately once every 10 miles (averaged over the entire journey). The average speed for this specific case is approximately 50 mph as gathered from [35]. Using pods in Configuration 3 ID: 305, the reduction in drag was 2.07% at 50 mph. At this speed, 50% of fuel expenditure is due to overcoming aerodynamic drag [2], and so pods would increase fuel economy by approximately 1.04%.

The average fuel consumed per combination truck vehicle was 10,435 US gallons in 2018 [40]. Using the average cost of diesel in the US in 2023 at $3.83 per US gallon [41], the total cost of fuel equates to approximately $39,966 per vehicle. By applying pods in the specified circumstances to a fleet size of 10 vehicles, the total yearly savings are approximately $4136.49. As the fuel price is much higher in the United Kingdom at a cost of £1.77 per litre in 2022 [42], applying the same case study results in a total yearly saving of £7235.56 for 10 vehicles. Given that a gallon of diesel produces 10.19 kg of CO_2 [43], this would equate to a reduction in emissions of around 11,005 kg. Going further, at typical highway speeds of 70 mph, the pods were shown to reduce drag by 2.12%, and so when applied in these circumstances would save approximately 1.38% in fuel usage, given that 65% of fuel expenditure is due to overcoming aerodynamic drag at this speed [2].

V. Conclusions and Recommendations for Further Work

To conclude this research, it was shown that AeroHance pods can effectively reduce the aerodynamic drag force by up to 2.12% for a Class 8 tractor-trailer by modifying wake and vortex structures, thereby increasing the base pressure. The pod placement optimisation study highlighted that the best Configuration in terms of drag reduction is one which employs the setup as described in ID:305. The pods have been shown to offer a simpler, lighter, less invasive, and cheaper alternative to the conventional drag-reducing devices mentioned in this report.

To the author's knowledge, this report presents the most extensive study of flow control devices of this type applied to heavy vehicles. This assessment is based on the vast number of simulations conducted and the considerable amount of existing literature utilised to support analysis.

To understand how changing each parameter affected the aerodynamic performance of the vehicle, the pod placement optimisation study systematically varied one parameter at a time against a baseline Configuration. Combinations of these configurations were therefore not explored due to the vast amount of simulations doing so would have accounted to, and so potential remains for further drag reduction. Future studies could therefore implement neural networks to efficiently explore such multi-parameter combinations. The findings within this report would suit well to such a study, given that the parameter boundaries have been identified, with the exception of pod AoA.

Another avenue that could be explored is fluid-structure interaction (FSI) analysis for heavy vehicles equipped with non-solid side walls, such as curtain-sided trailers. By doing so, the effectiveness of pods appended to such a vehicle could be accurately analysed by coupling CFD with Finite Element Analysis (FEA), thereby allowing the deformation of the vehicle body under aerodynamic loads.

Acknowledgments

This work was supported by Dr. Chris Toomer of UWE. Her invaluable knowledge and support during this project is greatly appreciated. Dr. Rodrigo Azcueta, and Hugh Ward of Cape Horn Engineering also supported this work. Their expertise and resources were received with great appreciation. Lastly, the author would like to thank Bob Evans of AeroHance Pods for accepting the use of the Pod geometry and for his support in this project.

REFERENCES

[1] B. L. Storms, D. R. Satran, J. T. Heineck, and S. M. Walker, "A summary of the experimental results for a generic tractor-trailer in the ames research center 7-by 10-foot and 12-foot wind tunnels," NASA Ames Research Center, Tech. Rep. NASA/TM-2006-213489, 2006.

[2] R. McCallen, R. Couch, J. Hsu, F. Browand, M. Hammache, A. Leonard, M. Brady, K. Salari, W. Rutledge, J. Ross *et al.*, "Progress in reducing aerodynamic drag for higher efficiency of heavy duty trucks (class 7-8)," SAE Technical Paper 1999-01-2238, 1999. [Online]. Available: https://doi.org/10.4271/1999-01-2238

[3] H. Choi, J. Lee, and H. Park, "Aerodynamics of heavy vehicles," *Annual Review of Fluid Mechanics*, vol. 46, pp. 441–468, 2014. [Online]. Available: https://doi.org/10.1146/annurev-fluid-011212-140616

[4] H. Ritchie, "Cars, planes, trains: where do CO_2 emissions from transport come from?" *Our World in Data*, 2020. [Online]. Available: https://ourworldindata.org/co2-emissions-from-transport

[5] R. M. Wood, "Operationally-practical & aerodynamically-robust heavy truck trailer drag reduction technology," SAE Int. J. Commer. Veh. 1(1):237-247, 2009. [Online]. Available: https://doi.org/10.4271/2008-01-2603

[6] J. Leuschen and K. R. Cooper, "Full-scale wind tunnel tests of production and prototype, second-generation aerodynamic drag-reducing devices for tractor-trailers," SAE Technical Paper 2006-01-3456, 2006. [Online]. Available: https://doi.org/10.4271/2006-01-3456

[7] K. Horrigan, B. Duncan, P. Sivakumar, A. Gupta, and A. Wong, "Aerodynamic simulations of a class 8 heavy truck: comparison to wind tunnel results and investigation of blockage influences," SAE Technical Paper 2007-01-4295, 2007. [Online]. Available: https://doi.org/10.4271/2007-01-4295

[8] M. V. Krishna and C. V. Ram, "Adjustable roof fairing for truck aerodynamics," SAE Technical Paper 2011-26-0106, 2011. [Online]. Available: https://doi.org/10.4271/2011-26-0106

[9] R. Simpson, "Trailer Side Skirts," Transport Engineer. Accessed: Mar. 14, 2025. [Online]. Available: https://www.transportengineer.org.uk/content/features/trailer-side-skirts/.

[10] R. Owens, "Regulations Now Permit Boat-tails But Should You Adopt Them?" Accessed: Mar. 17, 2025. [Online]. Available: https://donbur.co.uk/news/regulations/regulations-now-permit-aerodynamic-boat-tails.html.

[11] Driver & Vehicle Standards Agency and Department for Transport, "Retractable or foldable aerodynamic rear devices on heavy goods vehicles," Transport, Freight, Haulage and Cargo, Road Haulage. Accessed Mar. 21, 2025. [Online]. Available: https://www.gov.uk/guidance/retractable-or-foldable-aerodynamic-rear-devices-on-heavy-goods-vehicles.

[12] National Wind Tunnel Facility (NWTF), "The future of freight: NWTF team design AI-assisted, moveable flaps to cut aerodynamic drag on trucks," Accessed: Apr. 3, 2025. [Online]. Available: https://www.nwtf.ac.uk/case-study/the-future-of-freight-nwtf-team-design-ai-assisted-moveable-flaps-to-cut-aerodynamic-drag-on-trucks/.

[13] W. Lanier, *Transportation Technology*. Weigl Publishers Incorporated, 2019. [Online]. Available: https://books.google.co.uk/books?id=7L-2DwAAQBAJ

[14] W. Ke, I. Hashem, W. Zhang, and B. Zhu, "Influence of leading-edge tubercles on the aerodynamic performance of a horizontal-axis wind turbine: A numerical study," *Energy*, vol. 239, p. 122186, 2022. [Online]. Available: https://doi.org/10.1016/j.energy.2021.122186

[15] R. Supreeth, S. K. Maharana, and K. Bhaskar, "Whale inspired tubercles for passively enhancing the performance of a wind turbine blade," *International Journal of Renewable Energy Research-IJRER*, vol. 13, no. 1, 2023. [Online]. Available: https://doi.org/10.20508/ijrer.v13i1.12713.g8707

[16] AeroHance, "Nature Inspires Innovation," Accessed: Nov. 5, 2024. [Online]. Available: https://aerohance.com/technology/inspiration-whale-of-an-idea/.

[17] ——, "AeroHance Pod Performance by Vehicle Body Type," Accessed: Nov. 5, 2024. [Online]. Available: https://aerohance.com/performance/.

[18] Siemens Digital Industries Software, "Simcenter STAR-CCM+, version 2402," Siemens 2024. [Online]. Available: https://plm.sw.siemens.com/en-US/simcenter/fluids-thermal-simulation/star-ccm/

[19] Z. MacChesney, "Generic Conventional Model (GCM)," GrabCAD, 2016, Accessed Nov. 19, 2024. [Online]. Available: https://grabcad.com/library/generic-conventional-model-gcm-1.

[20] Siemens Digital Industries Software, "External Aerodynamics with Simcenter STAR-CCM+: Best practice guidelines (2406)," PDF presentation, Available via Siemens Support Portal, 2024.

[21] W. D. Pointer, T. Sofu, and D. Weber, "Development of Guidelines for the Use of Commercial CFD in Tractor-Trailer Aerodynamic Design," SAE Technical Paper 2005-01-3513, 2005. [Online]. Available: https://doi.org/10.4271/2005-01-3513

[22] Y. A. Çengel and J. M. Cimbala, *Fluid Mechanics: Fundamentals and Applications*, 3rd ed. McGraw Hill, 2013, p. 574.

[23] D. G. Hyams, K. Sreenivas, R. Pankajakshan, D. S. Nichols, W. R. Briley, and D. L. Whitfield, "Computational simulation of model and full scale class 8 trucks with drag reduction devices," *Computers Fluids*, vol. 41, no. 1, pp. 27–40, 2011. [Online]. Available: https://doi.org/10.1016/j.compfluid.2010.09.015

[24] F. R. Menter, "Two-equation eddy-viscosity turbulence models for engineering applications," *AIAA Journal*, vol. 32, no. 8, pp. 1598–1605, 1994. [Online]. Available: https://doi.org/10.2514/3.12149

[25] "Procedure for Estimation and Reporting of Uncertainty Due to Discretization in CFD Applications," *Journal of Fluids Engineering*, vol. 130, no. 7, p. 078001, 2008. [Online]. Available: https://doi.org/10.1115/1.2960953

[26] International Towing Tank Conference (ITTC), "Uncertainty Analysis in CFD, Examples for Resistance and Flow," ITTC Recommended Procedures and Guidelines 7.5-03-02-01, 2017. [Online]. Available: https://www.ittc.info/media/8161/75-03-02-01.pdf

[27] S. Evans and S. Lardeau, "Validation of a turbulence methodology using the SST k-ω model for adjoint calculation," AIAA 2016-0585. 54th AIAA Aerospace Sciences Meeting, January 2016. [Online]. Available: https://doi.org/10.2514/6.2016-0585

[28] W. D. Pointer and S. Singh, "Heavy vehicle drag estimation using commercial cfd tools," Presented at the Heavy Vehicle Systems Optimization Program Review, Argonne National Laboratory, April 2006.

[29] SAE International Recommended Practice, "Guidelines for Aerodynamic Assessment of Medium and Heavy Commercial Ground Vehicles Using Computational Fluid Dynamics," SAE Standard J2966_202106, Revised June 2021, Issued September 2013. [Online]. Available: https://doi.org/10.4271/J2966_202106

[30] Siemens Digital Industries Software, "Simcenter STAR-CCM+ User Guide, version 2402," in *Gamma ReTheta Transition Model*. Siemens, 2024, pp. 4573–4579.

[31] K. Ermiş, M. Çalışkan, and A. Okan, "The effects of surface roughness on the aerodynamic drag coefficient of vehicles," *International Journal of Automotive Science And Technology*, vol. 6, no. 2, p. 189–195, 2022. [Online]. Available: https://doi.org/10.30939/ijastech..1108956

[32] ANSYS, Inc., "Visualizing Laminar and Turbulent Regimes in a Transitional Simulation," https://innovationspace.ansys.com/courses/courses/topics-in-turbulence-modeling-using-ansys-cfx/lessons/visualizing-laminar-and-turbulent-regimes-in-a-transitional-simulation/, 2017.

[33] J. B. Barlow, R. Guterres, and R. Ranzenbach, "Experimental parametric study of rectangular bodies with radiused edges in ground effect," *Journal of Wind Engineering and Industrial Aerodynamics*, vol. 89, no. 14, pp. 1291–1309, 2001, bluff Body Aerodynamics and Applications. [Online]. Available: https://doi.org/10.1016/S0167-6105(01)00146-5

[34] J. J. Keller Compliance Network, "Speed limits - maximum for commercial motor vehicles (state comparison)," Accessed Dec. 11, 2024. [Online]. Available: https://jjkellercompliancenetwork.com/regsense/speed-limits-maximum-for-commercial-motor-vehicles-state-comparison-2656881725.

[35] National Renewable Energy Laboratory, 2014, "Fleet DNA Project Data." National Renewable Energy Laboratory, Transportation and Mobility Research, Fleet DNA: Commercial Fleet Vehicle Operating Data. [Online]. Available: http://www.nrel.gov/fleetdna.

[36] Siemens Digital Industries Software, "Simcenter STAR-CCM+ User Guide, version 2402," in *Flow Field Functions Reference*. Siemens, 2024, p. 3934.

[37] T. Khan, L. Pastur, O. Cadot, and V. Parezanović, "Equilibrium of fluid fluxes in the wake of a three-dimensional flat-back bluff body," *Journal of Fluid Mechanics*, vol. 997, p. A60, 2024. [Online]. Available: https://doi.org/10.1017/jfm.2024.614

[38] R. P. Littlewood and M. A. Passmore, "Aerodynamic drag reduction of a simplified squareback vehicle using steady blowing," *Experiments in Fluids*, vol. 53, no. 2, pp. 519–529, 2012. [Online]. Available: https://doi.org/10.1007/s00348-012-1306-4

[39] D. Bao, J. Borée, Y. Haffner, and C. Sicot, "Near wake interactions and drag increase regimes for a square-back bluff body," *Journal of Fluid Mechanics*, vol. 936, p. A2, 2022. [Online]. Available: https://doi.org/10.1017/jfm.2022.28

[40] U.S. Department of Transportation, Federal Highway Administration, 2018, "Annual Vehicle Distance Traveled in Miles and Related Data - 2018," Office of Highway Policy Information, Highway Statistics. [Online]. Available: https://www.fhwa.dot.gov/policyinformation/statistics/2018/vm1.cfm.

[41] U.S. Department of Energy, 2024, "Average Retail Fuel Prices in the United States," U.S. Department of Energy, Alternative Fuels Data Centre. [Online]. Available: https://afdc.energy.gov/fuels/prices.html.

[42] Agriculture and Horticulture Development Board (AHDB), “Fuel prices,” Accessed: Apr. 5, 2025. [Online]. Available: https://ahdb.org.uk/fuel-prices.

[43] U.S. Energy Information Administration - EIA, “Carbon dioxide emissions coefficients,” Accessed Feb. 3, 2025. [Online]. Available: https://www.eia.gov/environment/.

APPENDIX A
MODEL-SCALE SIMULATIONS

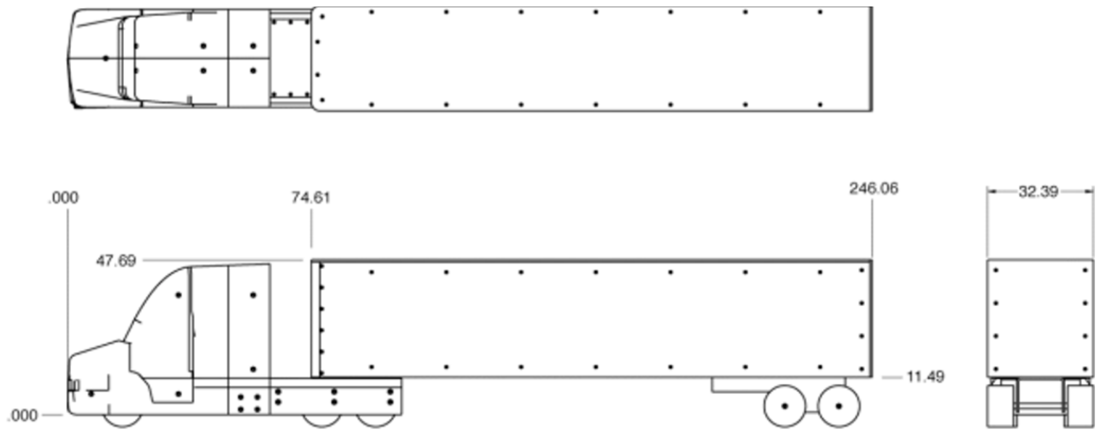

Fig. 21. GCM Model-Scale Geometry (All Dimensions in cm) [1]

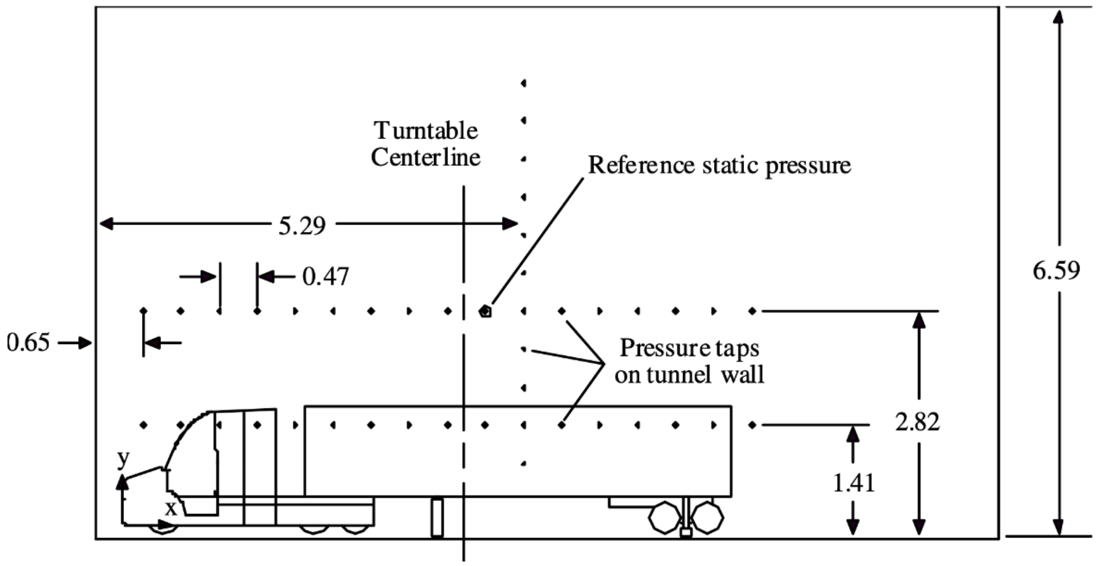

Fig. 22. Locations of Pressure Taps on Wind Tunnel Wall, with Specific Relevance to the Reference Static Pressure Probe. All Measurements are Normalised by Trailer Width. [1]

Appendix B
Full-Scale Simulations

The figures displayed within this appendix are from Configurations 0 & 3 (ID:305) unless stated otherwise, and serve as an example of the scenes and plots that helped draw the conclusions made within this report for all configurations. Due to the number of simulations carried out and the vast number of plots and scenes created, it was not possible to include them all within this appendix, although they are attached to this submission.

TABLE VI
Full-Scale Design of Experiments

Configuration	**ID**	**Velocity (m/s)**	**Pod Location**	**Pod Spacing[a] (m)**	**Pod Distance from TE[b] (m)**	**Side Pod AoA[c]**	**Roof Pod AoA[d]**
Config_0	001	17.88	N/A	N/A	N/A	N/A	N/A
	002	22.35	N/A	N/A	N/A	N/A	N/A
	003	26.82	N/A	N/A	N/A	N/A	N/A
	004	31.29	N/A	N/A	N/A	N/A	N/A
Config_1 (Pod Baseline)	101	26.82	Side+Roof	0.1016	0.254	0	0
Config_2	201	-	Side Only	-	-	-	-
	202	-	Roof Only	-	-	-	-
Config_3	301	-	-	-	0.127	-	-
	302	-	-	-	0.381	-	-
	303	-	-	-	6.840	-	-
	304	-	-	-	13.255	-	-
	305	-	-	-	0.050	-	-
Config_4	401	-	-	0.127	-	-	-
	402	-	-	0.1524	-	-	-
Config_5	501	-	-	-	-	-	LE Inboard 5°
	502	-	-	-	-	-	TE Inboard 5°
	503	-	-	-	-	LE Inboard 5°	-
	504	-	-	-	-	TE Inboard 5°	-
	505	-	-	-	-	+ 5°	-
	506	-	-	-	-	- 5°	-
Config_VelStudy	701	17.88	-	-	0.05	-	-
	702	22.35	-	-	0.05	-	-
	703	-	-	-	0.05	-	-
	704	31.29	-	-	0.05	-	-

[-] A dash indicates the parameter is the same as Config_1 (Pod Baseline).
[a] Distance Between Pod Centres (0,1,0 in Pod_CS).
[b] Lateral distance from the Trailing Edge of the Trailer to Pod Origin, Located Approximately One-Third of the Pod Length from the Pod Leading Edge.
[c] Angle of Attack of Side Pods (0,0,1 in Pod_Side_CS).
[d] Angle of Attack of Roof Pods (0,0,1 in Pod_Roof_CS).

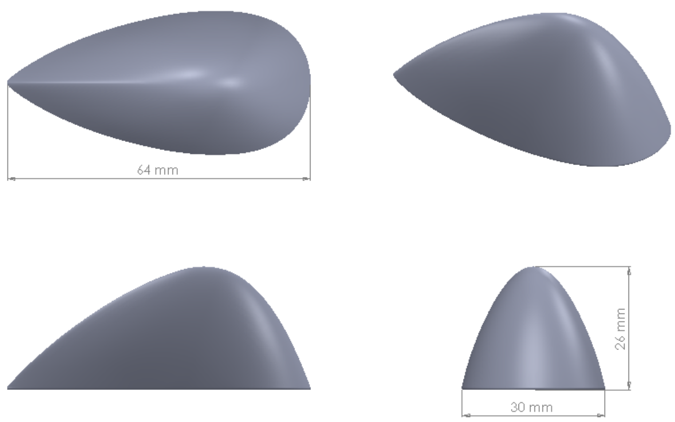

Fig. 23. AeroHance Pod Geometry

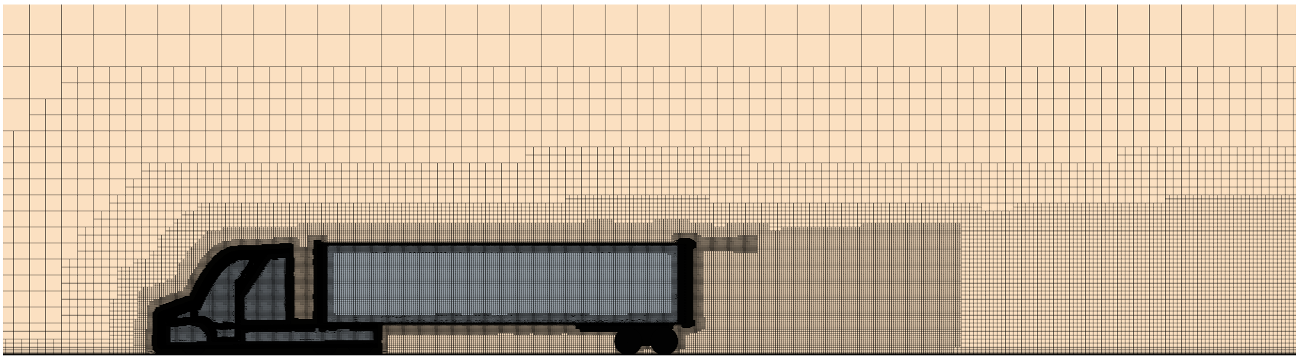

(a) Mesh Details - Side View, XZ Centreline Plane

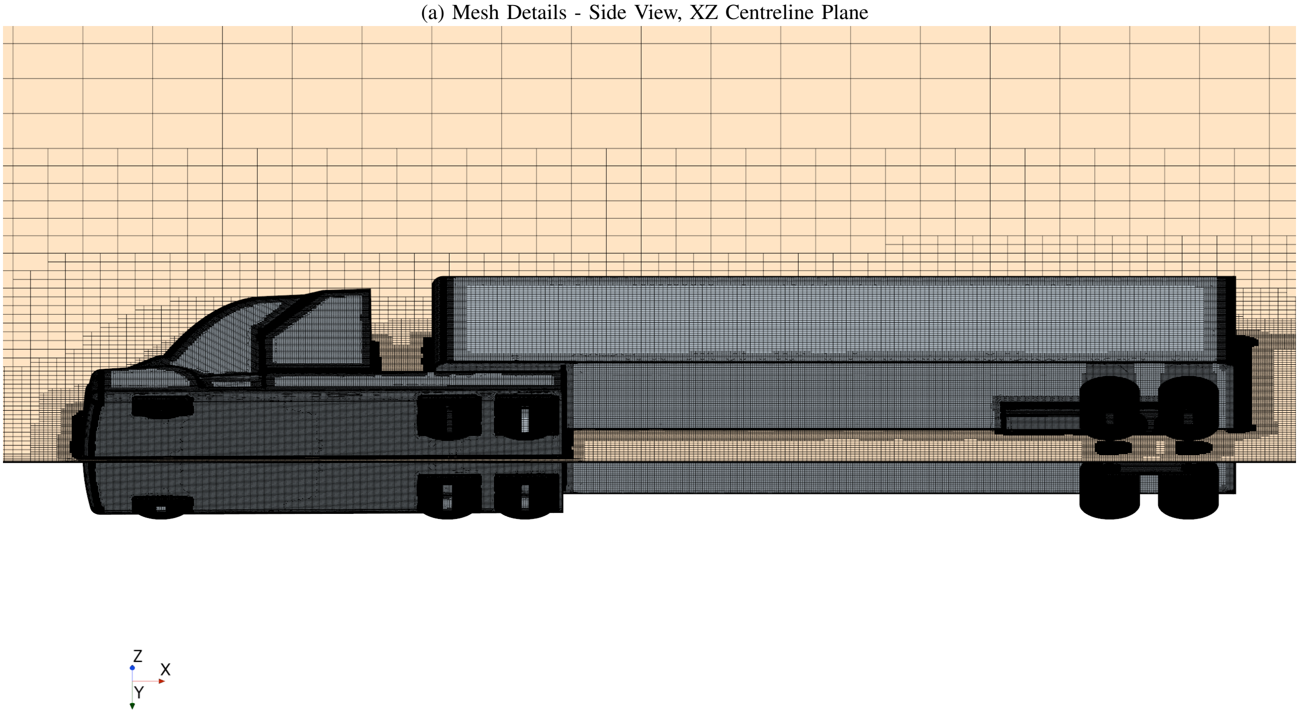

(b) Mesh Details - Bottom View, XZ Centreline Plane. Note: Holes on the Bottom of the Wheels are due to Floor-Tyre Intersection.

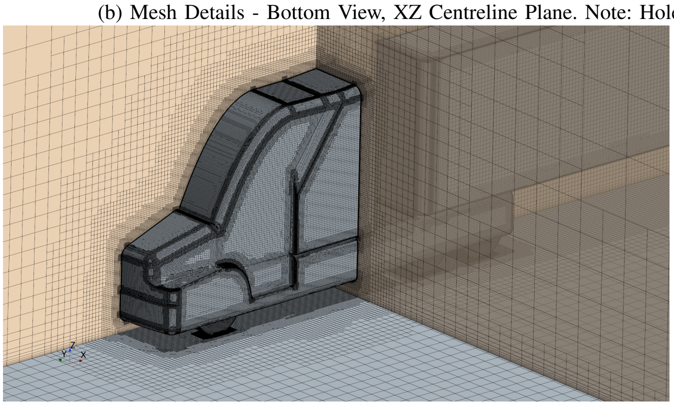

(c) Mesh Details - Front ISO View, XZ Centreline Plane, YZ Cut Plane Through Tractor Rear Section

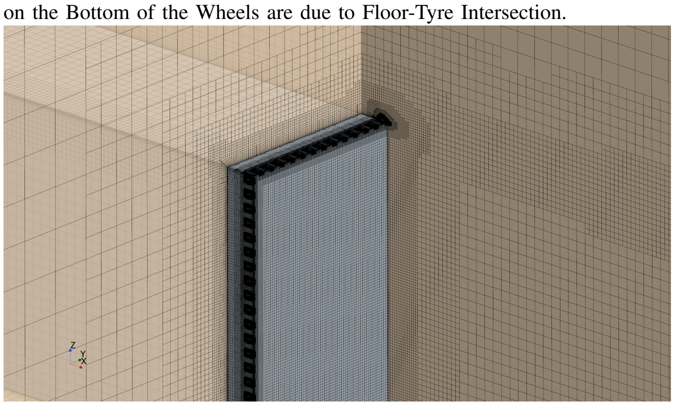

(d) Mesh Details - Rear ISO View, XZ Centreline Plane, YZ Cut Plane Through Trailer Rear Section

Fig. 24. Example Full-Scale Mesh: Config_3, ID:305.

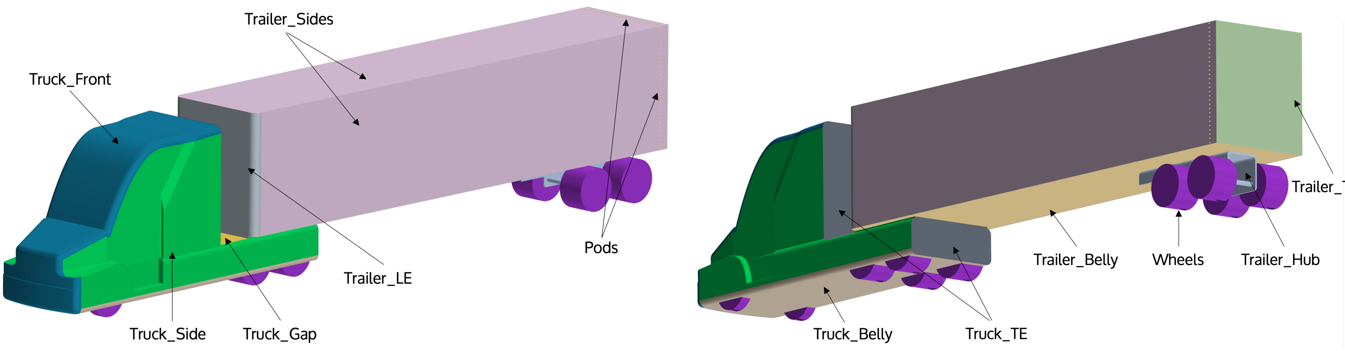

Fig. 25. Config_1: Description of Surface Identities (Representative of all Configurations)

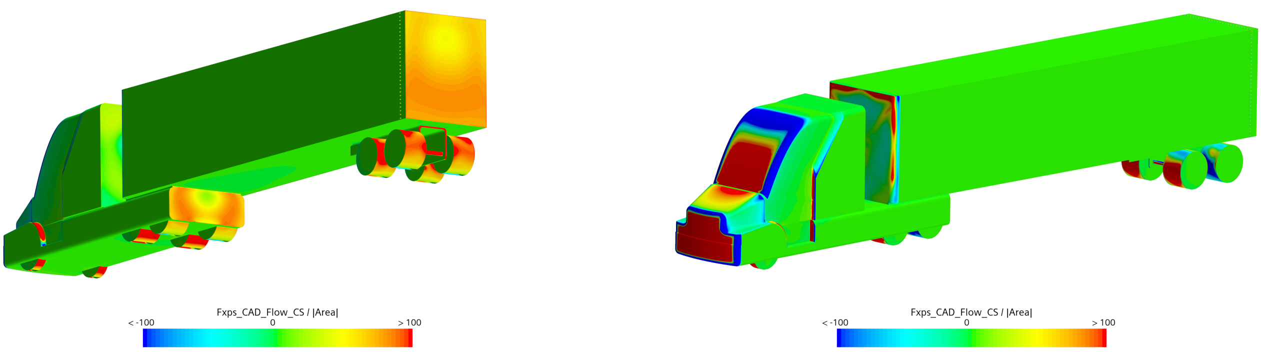

Fig. 26. Config_1:101 - Local Drag (Pressure+Shear Combined at Each Surface Cell), Summing to a Total Vehicle Drag of 1762 N

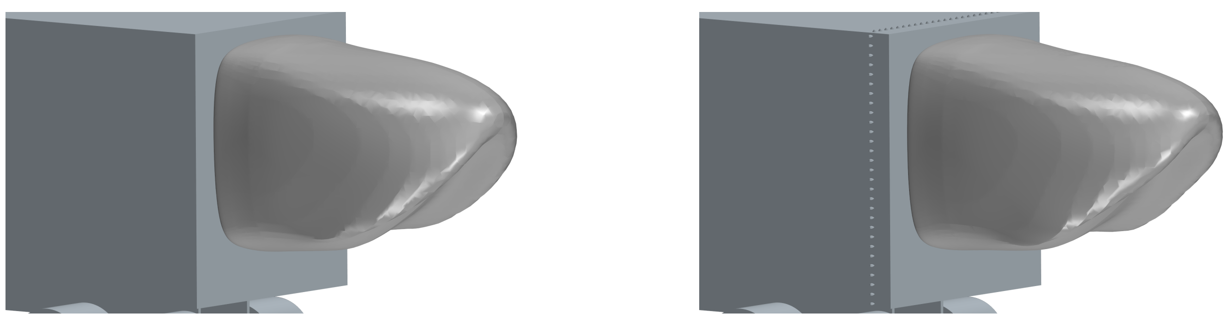

(a) Config_0 - ID:003

(b) Config_5 - ID:505

Fig. 27. Trailer (Light Grey) with Attached Flow Recirculation Bubble (Dark Grey), Identified by Isosurface of Velocity[i] = 0 m/s

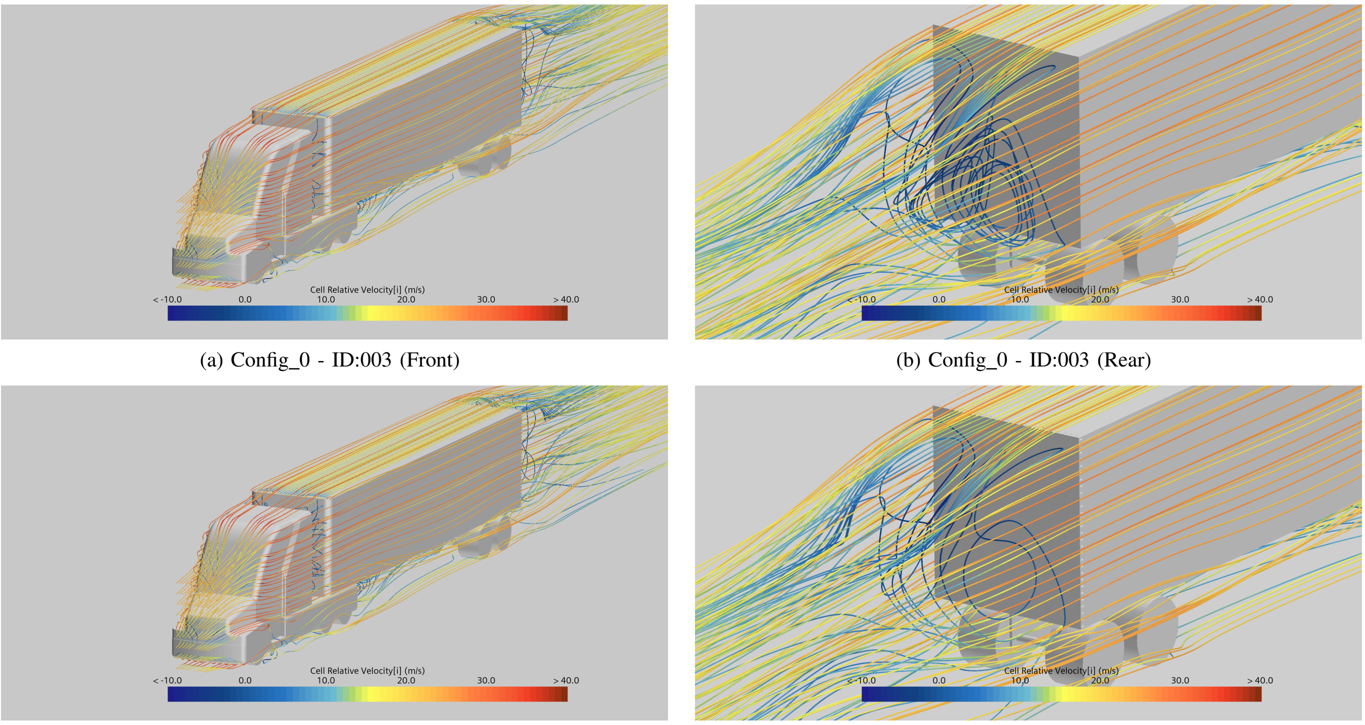

(a) Config_0 - ID:003 (Front)

(b) Config_0 - ID:003 (Rear)

(c) Config_3 - ID:305 (Front)

(d) Config_3 - ID:305 (Rear)

Fig. 28. Streamlines Displaying Cell Relative Velocity[i], Streamline Seed Positioned at the Front of the Tractor. Note the Large Turbulent, Asymmetric Recirculation Region in the Trailer Wake, with Improvement Seen When Pods are Appended.

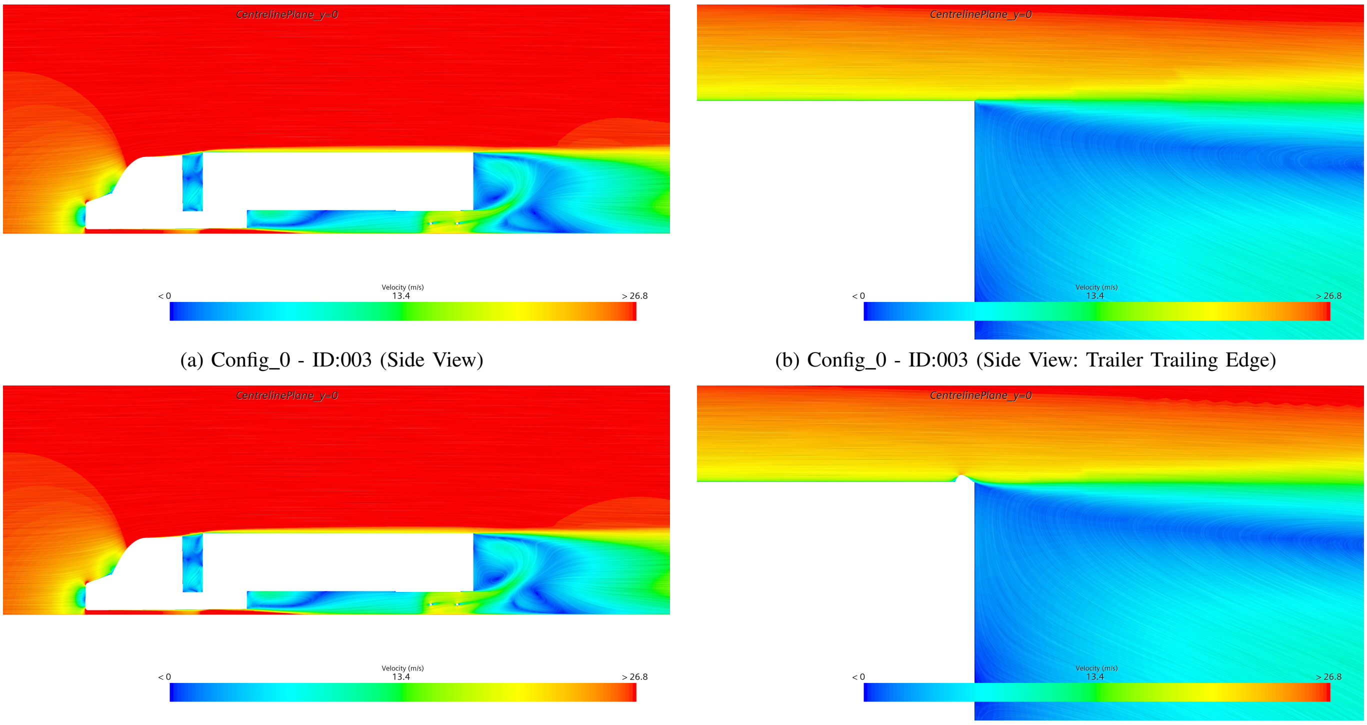

(a) Config_0 - ID:003 (Side View)

(b) Config_0 - ID:003 (Side View: Trailer Trailing Edge)

(c) Config_3 - ID:305 (Side View)

(d) Config_3 - ID:305 (Side View: Trailer Trailing Edge)

Fig. 29. LIC Displayer on Centreline Plane, Showing Velocity Magnitude

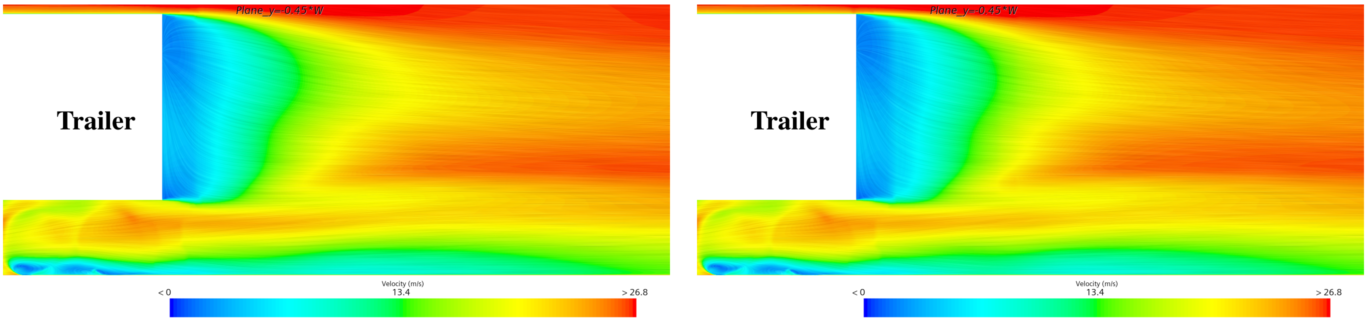

(a) Config_0 - ID:003 (b) Config_3 - ID:305

Fig. 30. LIC Displayer on XZ Plane Section at Y = -0.49 * Trailer Width, Showing Velocity Magnitude

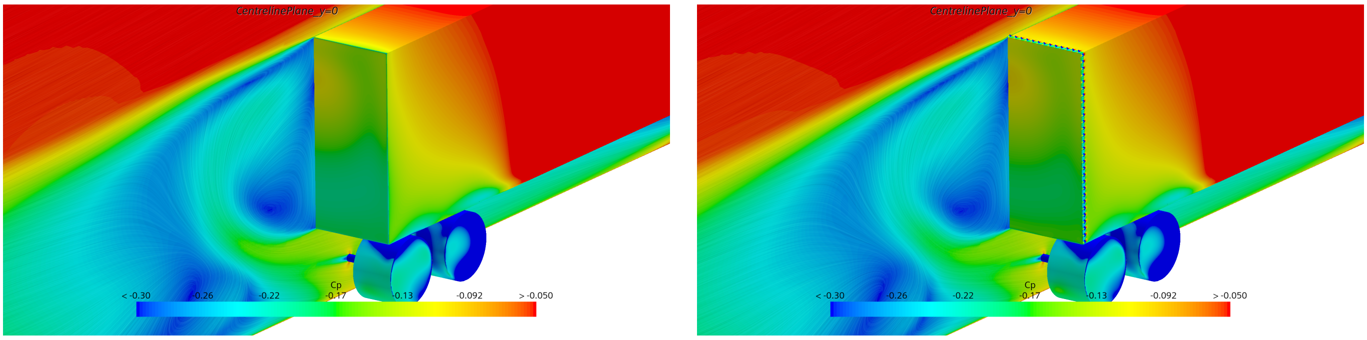

(a) Config_0 - ID:003 (b) Config_3 - ID:305

Fig. 31. Pressure Coefficient (ISO Rear View), with LIC Displayer on Centreline Plane Showing Velocity Magnitude

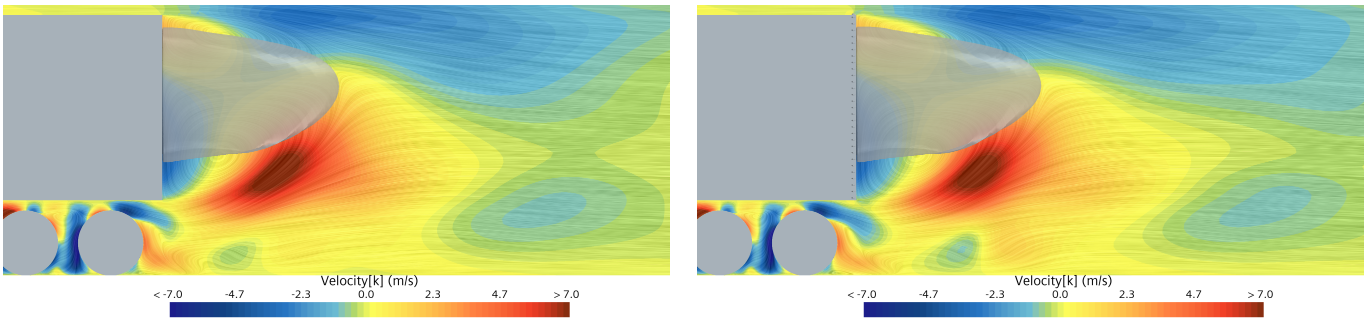

(a) Config_0 - ID:003 (b) Config_3 - ID:305

Fig. 32. Isosurface Acting on Velocity[i] = 0 to Highlight Recirculation Bubble, with XZ Plane Section at Y = -0.225 * Trailer Width, Displaying LIC with Velocity as Vector Field, Coloured by Velocity[k]

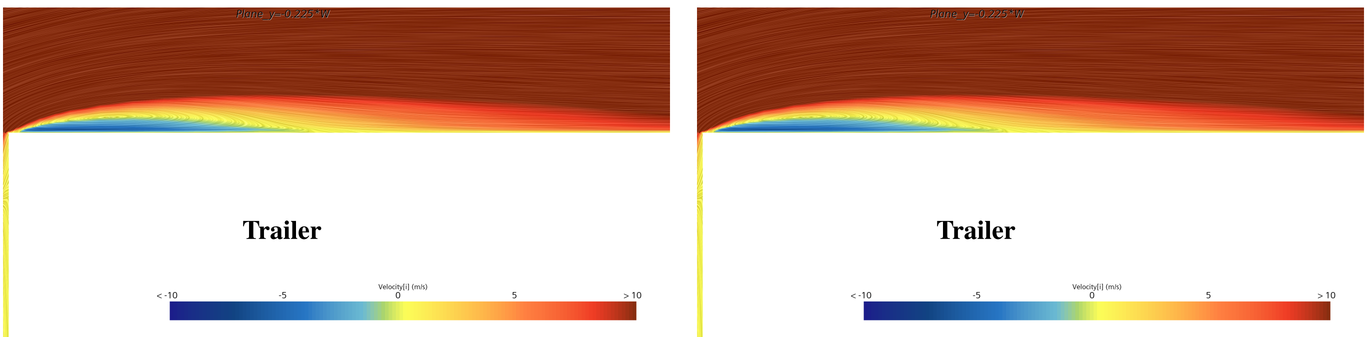

(a) Config_0 - ID:003 (b) Config_3 - ID:305

Fig. 33. XZ Plane Section at Y = -0.225 * Trailer Width, Displaying LIC with Velocity as Vector Field, Coloured by Velocity[i]. View at Trailer Leading Edge to Display Small Recirculating Separation Region

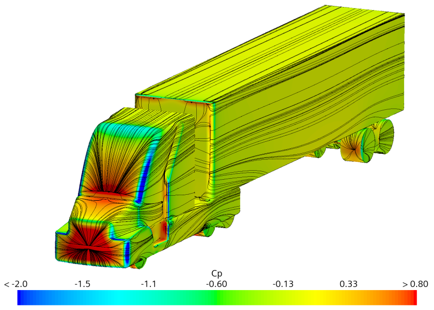

(a) Config_0 - ID:003

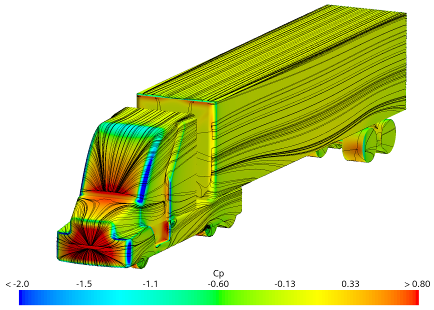

(b) Config_3 - ID:305

Fig. 34. Pressure Coefficient (ISO Front View), with Constrained Streamlines (Randomised)

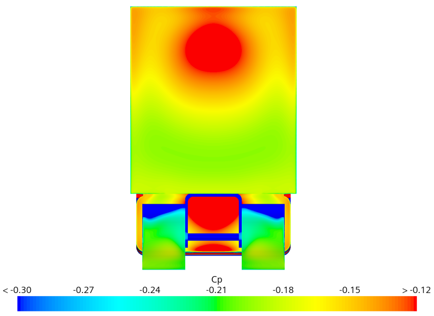

(a) Config_0 - ID:003

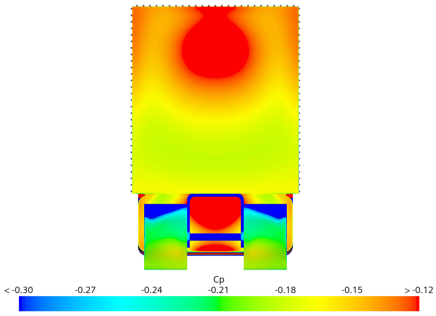

(b) Config_3 - ID:305

Fig. 35. Pressure Coefficient (Rear View)

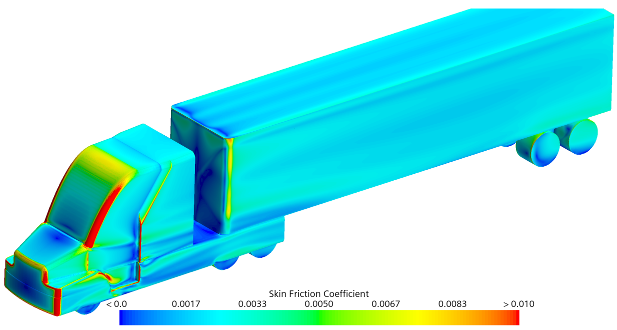

(a) Config_0 - ID:003

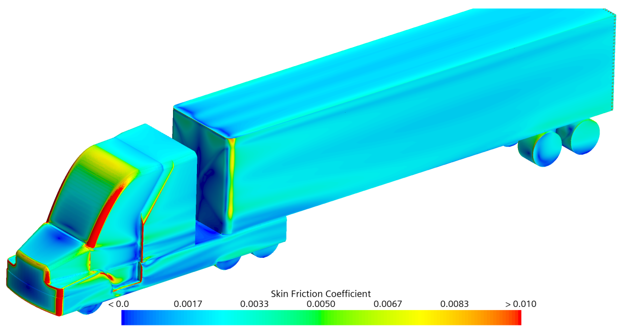

(b) Config_3 - ID:305

Fig. 36. Skin Friction Coefficient (ISO Front View)

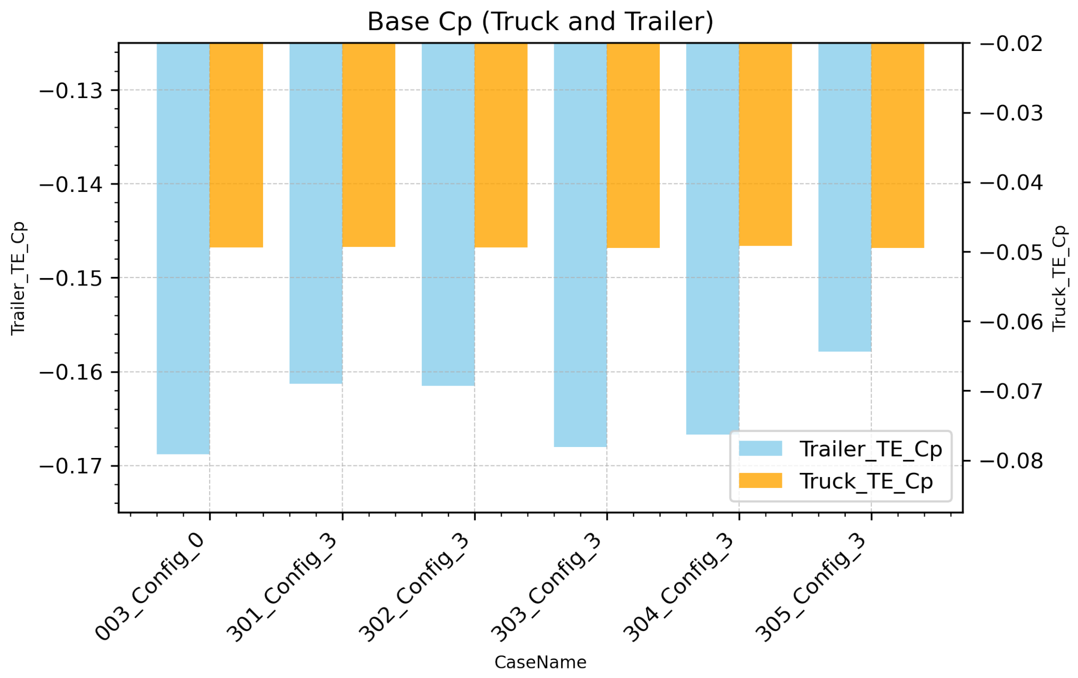

Fig. 37. Configurations 0 & 3: Tractor and Trailer Base C_p

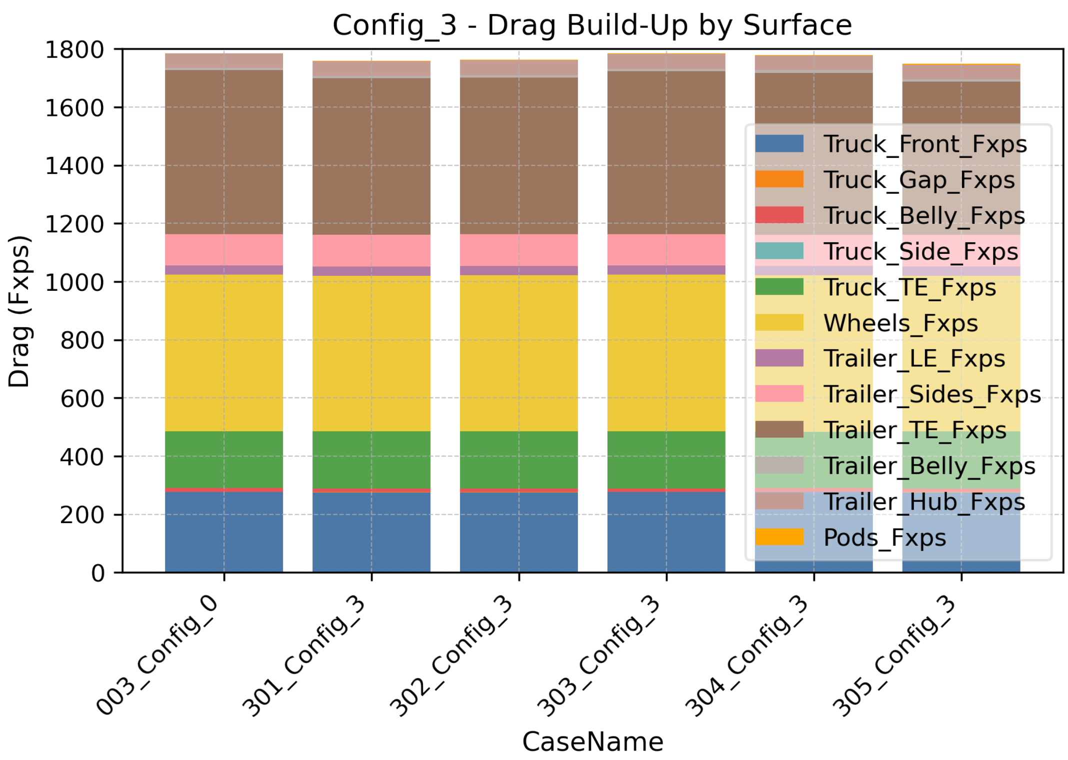

Fig. 38. Configurations 0 & 3: Drag Build-up by Surface

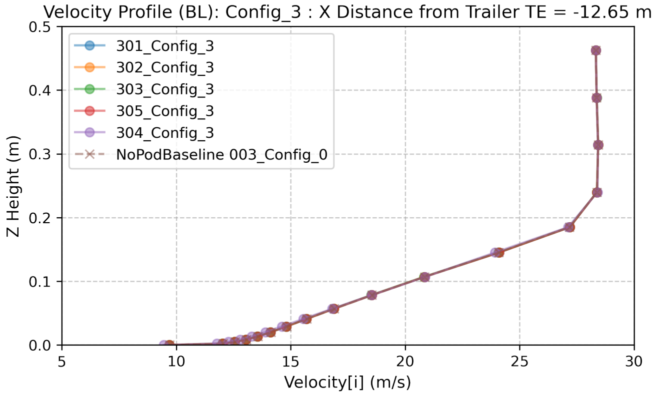

(a) X = -12.65 m From Trailer TE (60 cm Downstream of Pods in ID:304)

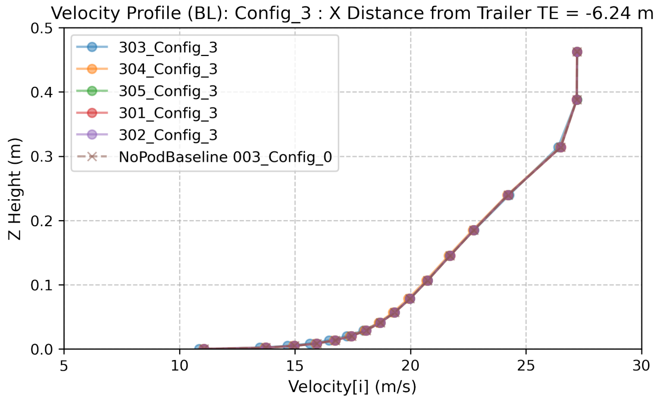

(b) X = -6.24 m From Trailer TE (60 cm Downstream of Pods in ID:303)

Fig. 39. Configurations 0 & 3: Trailer Centreline: Boundary Layer Velocity Profile

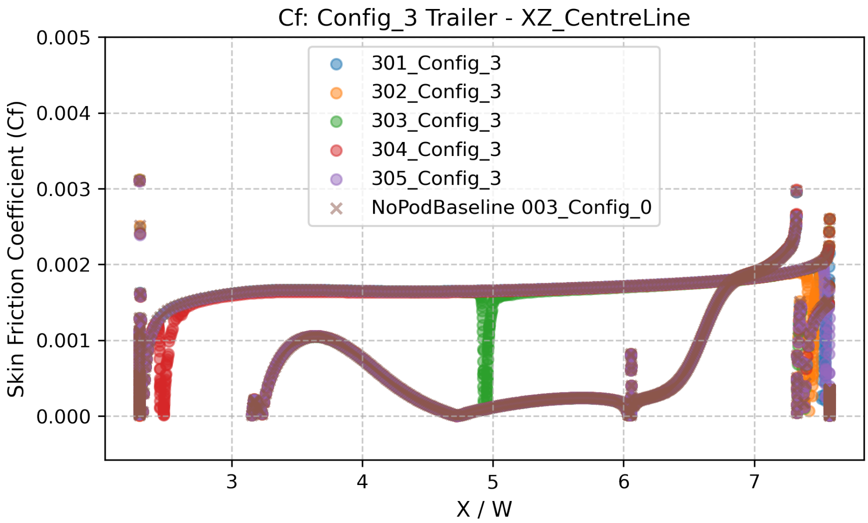

Fig. 40. Configuration 0 & 3: Skin Friction Coefficient Along Trailer Centreline

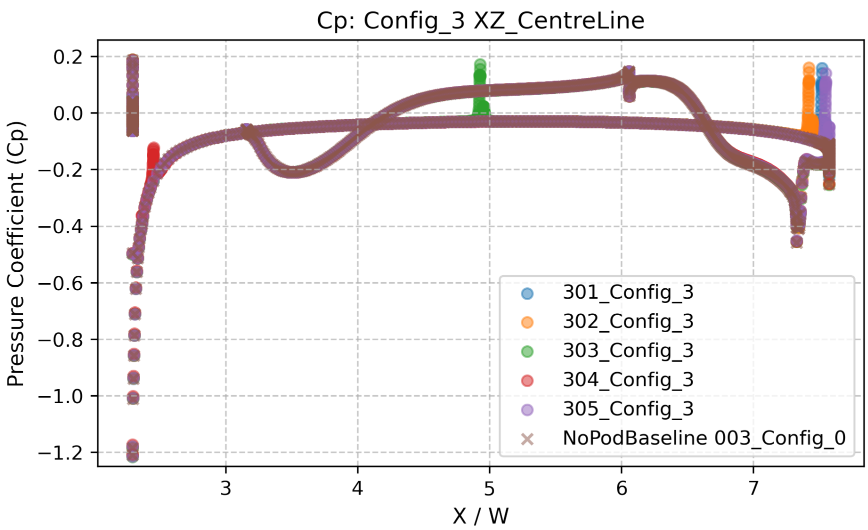

Fig. 41. Configuration 0 & 3: Pressure Coefficient Along Trailer Centreline

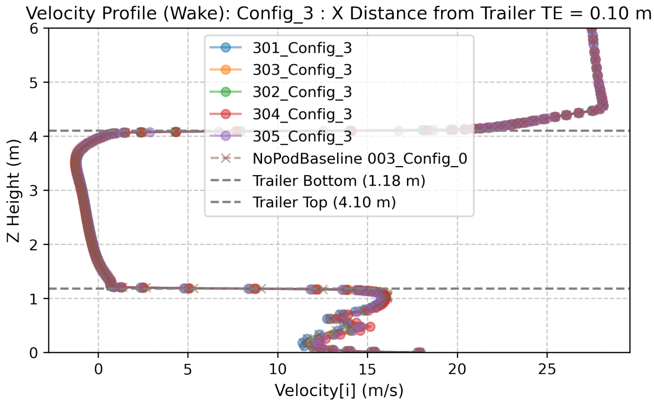

(a) X = 0.1 m Downstream of Trailer TE

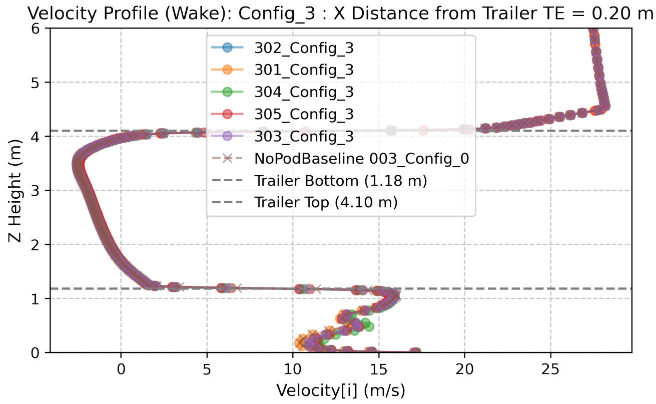

(b) X = 0.2 m Downstream of Trailer TE

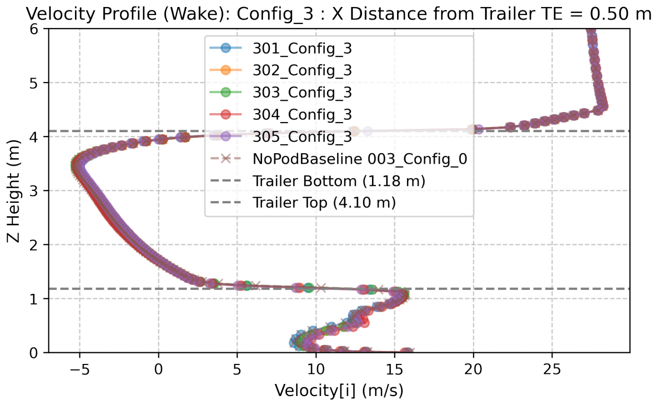

(c) X = 0.5 m Downstream of Trailer TE

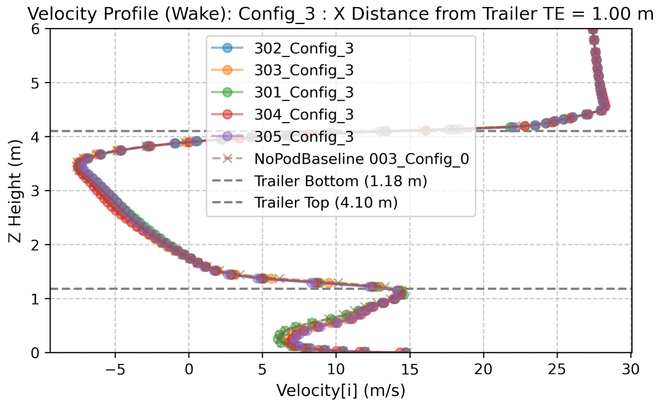

(d) X = 1 m Downstream of Trailer TE

Fig. 42. Configuration 0 & 3: Line Probes Positioned at Various x Distances from Trailer TE, Displaying the Velocity Profile Within the Wake